Department of Geography and Atmospheric Science
University of Kansas
1475 Jayhawk Boulevard
Lawrence, KS 66045
Email: bpu@ku.edu

Dr. Yves Balkanski
Institut Pascal et
IPSL/LSCE (Laboratoire des Sciences du Climat et de l'Environnement)
CEA-CNRS-UVSQ-UPSaclay UMR 8212
L'Orme des Merisiers - Bat 714, pce 1012
91191 Gif sur Yvette Cedex, FRANCE

November 21st, 2019

Dear Editor Balkanski,

Your helpful comments are sincerely appreciated. We have submitted a revised paper entitled "Retrieving the global distribution of threshold of wind erosion from satellite data and implementing it into the GFDL AM4.0/LM4.0 model" by B. Pu, P. Ginoux and co-authors to address these comments. We also made a few minor edits in the text.

We gratefully appreciate your time and consideration!

Sincerely,

Bing Pu

We sincerely appreciate the helpful comments from the Co-Editor. We reply to your comment (in Italic) below.

Comments to the Author:
The authors have adequately addressed the main concerns from the 2 reviewers by doing the additional sensitivity tests on soil moisture, LAI, snow coverage and threshold dust optical depth summarized in Table 2.
I would like the authors to add a sentence in the caption of Table 2 to explain the 2 different thresholds for DOD 0.2 (0.02) and 0.5 (0.05) depending on regions. This will help the reader understand this notation.

We added "Here DOD_{thresh}=0.2 or 0.5 is applied to dusty regions, i.e., the Sahel, Sahara, Arabian Peninsula, northern China, and India, while DOD_{thresh}=0.02 or 0.05 is applied to less dusty regions, i.e., the U.S., South Africa, South America, and Australia." To the caption of Table 2.

Now that Figure 9 (ex Fig. 8) is in log-scale, the correlation factors have changed, please check the value for these correlation factors.

Thanks for noticing this. We checked the correlation coefficients and other statistics in Fig. 9, and they are based on log-scale data. The correlation coefficient in the Control run (top left plot) looks the same as the previous version due to the precision level applied here. They are actually slightly different: the original correlation coefficient is 0.762638, and the correlation for the log-scale data is 0.756081.

Retrieving the global distribution of threshold of wind erosion from satellite data and implementing it into the GFDL AM4.0/LM4.0 model

Bing Pu[1, 2, *], Paul Ginoux[2], Huan Guo[2, 3], N. Christine Hsu[4], John Kimball[5], Beatrice Marticorena[6], Sergey Malyshev[2], Vaishali Naik[2], Norman T. O'Neill[7], Carlos Pérez García-Pando[8], Joseph M. Prospero[9], Elena Shevliakova[2], Ming Zhao[2]

[1]Atmospheric and Oceanic Sciences Program, Princeton University, Princeton, New Jersey 08544

[2] NOAA Geophysical Fluid Dynamics Laboratory, Princeton, New Jersey 08540

[3] Cooperative Programs for the Advancement of Earth System Science, University Corporation for Atmospheric Research, Boulder, Colorado, 80301

[4] NASA Goddard Space Flight Center, Greenbelt, Maryland, 20771

[5] Department of Ecosystem and Conservation Sciences, University of Montana, Missoula, Montana 59812

[6]LISA, Universités Paris Est-Paris Diderot-Paris

[7] Département de géomatique appliquée , Université de Sherbrooke

[8] Barcelona Supercomputing Center, Barcelona, Spain, 08034

[9] Rosenstiel School of Marine and Atmospheric Sciences, University of Miami, Miami, Florida, 33149

[*] Current affiliation: Department of Geography~~Geographical~~ and Atmospheric Science, the University of Kansas, Lawrence, Kansas, 66045

Abstract. Dust emission is initiated when surface wind velocities exceed the threshold of wind erosion. Many dust models used constant threshold values globally. Here we use satellite products to characterize the frequency of dust events and land surface properties. By matching this frequency derived from Moderate Resolution Imaging Spectroradiometer (MODIS) Deep Blue aerosol products with surface winds, we are able to retrieve a climatological monthly global distribution of wind erosion threshold ($V_{threshold}$) over dry and sparsely-vegetated surface. This monthly two-dimensional threshold velocity is then implemented into the Geophysical Fluid Dynamics Laboratory coupled land-atmosphere model (AM4.0/LM4.0). It is found that the climatology of dust optical depth (DOD) and total aerosol optical depth, surface PM_{10} dust concentrations, and seasonal cycle of DOD are better captured over the "dust belt" (i.e. North Africa and the Middle East) by simulations with the new wind erosion threshold than those using the default globally constant threshold. The most significant improvement is the frequency distribution of dust events, which is generally ignored in model evaluation. By using monthly rather than annual mean $V_{threshold}$, all comparisons with observations are further improved. The monthly global threshold of wind erosion can be retrieved under different spatial resolutions to match the resolution of dust models and thus can help improve the simulations of dust climatology and seasonal cycle as well as dust forecasting.

1. Introduction

Mineral dust is one of the most abundant aerosols by mass and plays an important role in the climate system. Dust particles absorb and scatter solar and terrestrial radiation, thus modifying local energy budget and consequently atmospheric circulation patterns. Studies have shown that the radiative effect of dust can affect a wide range of environmental processes. Dust is shown to modulate West African (e.g., Miller and Tegen, 1998; Miller et al., 2004; Mahowald et al., 2010; Strong et al., 2015) and Indian (e.g., Jin et al., 2014; Vinoj et al., 2014; Jin et al., 2015; Jin et al., 2016; Solmon et al., 2015; Kim et al., 2016; Sharma and Miller, 2017) monsoonal precipitation. During severe droughts in North America, there is a positive feedback between dust and the hydrological cycle (Cook et al., 2008, 2009; 2013). African dust is also found to affect Atlantic tropical cyclone activities (e.g., Dunion and Velden, 2004; Wong and Dessler, 2005; Evan et al., 2006; Strong et al., 2018). When deposited on snow and ice, dust reduces the surface reflectivity, enhancing net radiation and accelerating snow and ice melting, and consequently affecting runoff (e.g., Painter et al., 2010; 2018; Dumont et al., 2014). Dust can serve as ice nuclei and affect the formation, lifetime, and characteristic of clouds (e.g., Levin et al., 1996; Rosenfield et al., 1997; Wurzler et al., 2000; Nakajima et al., 2001; Bangert et al., 2012), perturbing the hydrological cycle. Iron and phosphorus enriched dust is also an important nutrient for the marine and terrestrial ecosystems and thus interacts with the ocean and land biogeochemical cycles (e.g., Fung et al., 2000; Jickells et al., 2005; Shao et al., 2011; Bristow et al., 2010; Yu et al., 2015).

Given the importance of mineral dust, many climate models incorporate dust emission schemes to simulate the life cycle of dust aerosols (e.g., Donner et al., 2011;

47 Collins et al., 2011; Watanabe et al., 2011; Bentsen et al., 2013). Mineral dust particles
48 are lifted from dry and bare soils into the atmosphere by saltation and sandblasting. This
49 process is initiated when surface winds reach a threshold velocity of wind erosion. The
50 value of this wind erosion threshold depends on soil and surface characteristics, including
51 soil moisture, soil texture and particle size, and presence of pebbles, rocks, and
52 vegetation residue (e.g., Gillette et al., 1980; Gillette and Passi, 1988; Raupach et al.,
53 1993; Fécan et al., 1999; Zender et al., 2003; Mahowald et al., 2005), and thus varies
54 spatially and temporally (Helgren and Prospero, 1987). Due to a lack of in-situ data at
55 global scale and uncertainties on these dependencies, most dust and climate models
56 prescribe a spatially and temporally constant threshold of wind erosion for surface 10 m
57 wind (e.g., around 6 to 6.5 m s^{-1}) over dry surface for simplicity (e.g., Tegen and Fung,
58 1994; Takemura et al., 2000; Uno et al., 2001; Donner et al., 2011). For instance, in the
59 Geophysical Fluid Dynamics Laboratory coupled land-atmosphere model AM4.0/LM4.0
60 (Zhao et al., 2018a, b), a constant threshold of 6 m s^{-1} is used. On the other hand, some
61 models, such as the ECHAM-HAM, HadGEM2-ES, and ICON-ART, parameterize the
62 constant dry threshold friction velocity (usually a function of soil particle size, soil and
63 air density) or threshold wind velocity with dependencies on soil moisture, surface
64 roughness length, and vegetation coverage (e.g., Takemura et al. 2000; Ginoux et al.
65 2001; Zender et al. 2003; Cheng et al., 2008; Jones et al., 2011; Rieger et al., 2017).
66 The threshold of wind erosion may be approximately inferred using observations.
67 For instance, Chomette et al. (1999) used the Infrared Difference Dust Index (IDDI) and
68 10 m winds reanalysis from the European Centre for Medium-Range Weather Forecasts
69 (ECMWF) between 1990 and 1992 to calculate the threshold of wind erosion over seven

sites over the Sahel and Sahara. The IDDI was used to determine whether there was a dust event for subsequently calculating an emission index defined as the number of dust events to the total number of potential events. The distribution of surface wind speed was matched with the emission index, and the threshold of wind erosion was determined when the emission index was around 0.9. The resulting average threshold of wind erosion ranged from 6.63 m s^{-1} at a Sahelian site to about 9.08 m s^{-1} at a Niger site, consistent with the model results by Marticorena et al. (1997).

Later, Kurosaki and Mikami (2007) used World Meteorological Organization (WMO) station data from March 1998 to June 2005 to examine the threshold wind speed in East Asia. Using the distribution of surface wind speed and associated weather conditions (i.e., with or without dust emission events), they approximated a dust emission frequency by dividing number of dust events to the total number of observations for each wind bin, and then determined threshold wind speeds at the 5% and 50% levels, corresponding to the most favorable and normal land surface conditions for dust emission, respectively. They found that the derived threshold wind speed varied in space and time, with a larger seasonal cycle in grassland regions, such as northern Mongolia, and smaller seasonal variations in desert regions, such as the Taklimakan and Gobi Deserts and the Loess Plateau. Cowie et al. (2014) applied a similar method over northern Africa, using wind data observed between 1984 and 2012, and focused on threshold winds at the 25%, 50%, and 75% levels.

Draxler et al. (2010) derived the distribution of threshold of ~~wind erosion~~friction velocity over the U.S. by matching the frequency of occurrence (FoO) of Moderate Resolution Imaging Spectroradiometer (MODIS) Deep Blue (Hsu et al., 2004) aerosol

optical depth (AOD) above 0.75 with the FoO of friction velocities extracted from the North American Mesoscale (NAM) forecast model at each grid point. This new threshold and a soil characteristics factor was then incorporated into the Hybrid Single-Particle Lagrangian Integrated Trajectory (HYSPLIT) model (Draxier and Hess, 1998) to forecast dust surface concentrations. It was found that major observed dust plume events in June and July 2007 were successfully captured by the model. Later, Ginoux and Deroubaix (2017) used FoO derived from the MODIS Deep Blue dust optical depth (DOD) record to retrieve the wind erosion threshold of surface 10 m winds over East Asia.

For individual dust events, the threshold of friction velocity can also be determined by fitting a second-order Taylor series to dust saltation flux measurements (Barchyn and Hugenholtz, 2011; Kok et al., 2014b).

Nonetheless, a global distribution of threshold of wind erosion with observational constraints that may be implemented in climate models is still lacking. In this study, we propose a method to retrieve monthly global threshold of wind erosion (hereafter, $V_{threshold}$) for dry and sparsely-vegetated surface (i.e., under favorable conditions for dust emission) using high-resolution satellite products and reanalysis datasets. This two-dimensional threshold of surface 10 m winds is then implemented into the Geophysical Fluid Dynamics Laboratory (GFDL) coupled land-atmosphere model, AM4.0/LM4.0 (Zhao et al., 2018a, b). The benefits of using this spatial and temporal varying threshold in simulating present-day climatology and seasonal cycles of dust are analyzed by comparing the model results with observations.

115 The data and method used to retrieve the threshold of wind erosion are detailed in
116 section 2. The distribution of the derived $V_{threshold}$ and its implication in the climate model
117 is presented in section 3. Section 4 discusses the uncertainties associated with this
118 method, and major conclusions are summarized in section 5.
119
120 **2. Data and Methodology**
121 In this section we first introduce the satellite products, observational data, and
122 reanalyses used to retrieve the threshold of wind erosion and validate model output
123 (section 2.1). The processes to retrieve the threshold of wind erosion are detailed in
124 section 2.2. The uncertainties of $V_{threshold}$ associated with the retrieval criteria and
125 selection of surface wind datasets are discussed in section 2.3. Section 2.4 introduces
126 GFDL AM4.0/LM4.0 model, its dust emission scheme, and simulation designs.
127
128 **2.1 Data**
129 **2.1.1 Satellite products**
130 1) MODIS Aqua and Terra dust optical depth
131 DOD is column-integrated extinction by mineral particles. Here daily DOD is
132 retrieved from MODIS Deep Blue aerosol products (collection 6, level 2; Hsu et al.,
133 2013; Sayer et al., 2013): aerosol optical depth (AOD), single-scattering albedo (ω), and
134 the Ångström exponent (α). All the daily variables are first interpolated to a 0.1° by 0.1°
135 grid using the algorithm described by Ginoux et al. (2010). We require that the single-
136 scattering albedo at 470 nm to be less than 0.99 for dust due to its absorption of solar
137 radiation. This separates dust from scattering aerosols, such as sea salt. Then a continuous

function relating the Ångström exponent, which is highly sensitive to particle size (Eck et al., 1999), to fine-mode AOD established by Anderson et al. (2005; their Eq. 5) is used to separate dust from fine particles. In short, DOD is retrieved using the following equation:

$$DOD = AOD \times (0.98 - 0.5089\alpha + 0.0512\alpha^2) \quad . \quad (1)$$

Details about the retrieval process and estimated errors are summarized by Pu and Ginoux (2018b). High-resolution MODIS DOD products (0.1° by 0.1°) have been used to identify and characterize dust sources (Ginoux et al., 2012; Baddock et al., 2016) and examine the variations in dustiness in different regions (e.g., Pu and Ginoux, 2016, 2017, 2018b).

Following the recommendation from Baddock et al. (2016), who found the dust sources are better detected using DOD with a low-quality flag (i.e., quality assurance flag, QA, equals 1, following the category of retrieval quality flags in MODIS Deep Blue products; Hsu et al., 2013) than that with a high-quality flag (i.e., QA=3) as retrieved aerosol products were poorly flagged over dust source regions, we also use DOD with the flag of QA=1. Both daily DOD retrieved from Aqua and Terra platforms are used by averaging the two when both products are available or using either one when only one product is available. Since Terra passes the equator from north to south around 10:30 am local time (LT) and Aqua passes the Equator from south to north around 13:30 pm LT, an average of the two combines the information from both morning and afternoon hours. This process also largely reduces missing data (Pu and Ginoux, 2018b). This combined daily DOD, hereafter MODIS DOD, is available from January 2003 to December 2015 at a resolution of 0.1° by 0.1° grid. Note that due to the temporal coverage of MODIS

products, the diurnal variations in dust (e.g., O'rgill and Sehmel, 1976; Mbourou et al., 1997; Knippertz, 2008; Schepanski et al., 2009) are not included in current study.

2) Soil moisture

Soil moisture is an important factor that affects dust emission (Fécan et al., 1999). Daily surface volumetric soil moisture (VSM) retrievals derived from similar calibrated microwave (10.7 GHz) brightness temperature observations from the Advanced Microwave Scanning Radiometer-Earth Observing System (AMSR-E) onboard the NASA Aqua satellite (from June 2002 to October 2011) and the Advanced Microwave Scanning Radiometer 2 (AMSR2) sensor onboard the JAXA GCOM-W1 satellite (from July 2012 to June 2017) from the University of Montana (Du et al., 2017a; Du et al., 2017b) was used to retrieve wind erosion threshold. Both AMSR-E and AMSR2 sensors provide global measurements of polarized microwave emissions at six channels, with ascending and descending orbits crossing the equator at around 1:30 pm and 1:30 am LT, respectively. The VSM retrievals are derived from an iterative retrieval algorithm that exploits the variable sensitivity of different microwave frequencies and polarizations, and minimizes the potential influence of atmosphere, vegetation, and surface water cover on the soil signal. The VSM record represents surface (top ~2 cm) soil conditions and shows favorable global accuracy and consistent performance (Du et al. 2017b), particularly over areas with low to moderate vegetation cover that are also more susceptible to wind erosion, although cautions are needed when examining long-term trends due to the small biases between AMSR-E and AMSR2. The horizontal resolution of the product is about 25 km by 25 km, and the daily product from January 2003 to December 2015 is used.

The ascending and descending obit VSM retrievals are averaged to get the mean VSM for each day.

3) Snow cover

Snow cover may affect dust emission in the mid-latitudes during spring, for instance, over northern China (Ginoux and Deroubaix, 2017). The interannual variation of snow cover is also found to affect dust emission in regions, such as Mongolia (Kurosaki and Mikami, 2004). Here monthly snow cover data from MODIS/Terra level 3 data (Hall and Riggs, 2015) with a resolution of 0.05° by 0.05° from 2003 to 2015 is used. The high spatial resolution of the product is very suitable for this study.

4) Leaf area index (LAI)

Vegetation protects soil from the effects of wind and thus modulates dust emission (e.g., Marticorena and Bergametti, 1995; Zender et al., 2003). While dense vegetation coverage can increase surface roughness and reduce near surface wind speed, the roots of vegetation can increase soil cohesion and further reduce wind erosion. LAI describes the coverage of vegetation with a unit of m^2/m^2, i.e., leaf area per ground area. Here monthly LAI retrieved by Boston University from MODIS onboard Aqua (Yan et al., 2016a; Yan et al., 2016b; via personal communication with Ranga Myneni and Taejin Park; Boston University, 2016) with a resolution of 0.1° by 0.1° from 2003 to 2015 is used. The root mean square error of the product is 0.66, with some overestimation of LAI in sparsely vegetated regions (Yan et al. 2016b; Garrigues et al., 2008).

206 **2.1.2 Reanalysis**

207 Surface wind speed is a critical factor that affects wind erosion. Here 6--hourly 10
208 m wind speed from the NCEP/NCAR reanalysis (Kalnay et al., 1996, hereafter NCEP1)
209 on a T62 Gaussian grid (i.e., 192 longitude grids equally spaced and 94 latitude grids
210 unequally spaced) is used. The NCEP1 is a global reanalysis with relatively long
211 temporal coverage, from 1948 to the present. We chose to use the NCEP1 reanalysis
212 mainly because surface winds in the GFDL AM4.0 model are nudged toward the NCEP1,
213 and we preferred to use the reanalysis surface wind that is closest to the model
214 climatology.

215 ERA-Interim (Dee et al., 2011) is a global reanalysis produced from ECMWF. It
216 provides high spatial resolution (about 0.75° or 80 km) 6-hourly, daily, and monthly
217 reanalysis from 1979 to present day. Soil temperature from the ERA-Interim is used to
218 determine the regions where wind erosion may be prohibited by the frozen surface.
219 Monthly temperature of the first soil layer (0 to 0.07 m) from 2003 to 2015 is used.

220 In order to quantify the uncertainties of the retrieved threshold wind erosion in
221 association with the selection of reanalysis products, surface 10 m winds from 6-hourly
222 ERA-Interim and hourly ERA5 (Hersbach and Dee, 2016) are both examined. The ERA5
223 is the latest reanalysis product from the ECMWF, with a horizontal resolution of about 31
224 km and hourly temporal resolution.

225

226 **2.1.3 Station data**

227 Multiple ground-based datasets are used to validate AM4.0/LM4.0 simulated
228 aerosol and dust optical depth and surface dust concentrations.

1) AERONET

The AErosol RObotic NETwork (AERONET; Holben et al., 1998) provides quality assured cloud-screened (level 2) aerosol measurements from sunphotometer records. In this paper we used the data products of the version 3.0 AERONET processing routine. To examine model simulated DOD, we used coarse mode AOD (COD; i.e., radius > 0.6 μm) at 500 nm processed by the Spectral Deconvolution Algorithm (O'Neill et al., 2003; hereafter SDA). SDA COD monthly data is first screened to remove those months with less than five days of records. To get the annual means, years with less than five months of records were removed. Only stations with records of at least three years during the period were used to calculate the 2003-2015 climatology (the same time period when MODIS DOD is available). Overall, records from 313 stations were obtained.

AERONET monthly aerosol optical thickness (AOT) data around 550 nm (e.g., 500 nm, 551 nm, 531 nm, 440 nm, 675 nm, 490 nm, 870 nm, etc.) and the Ångström exponents across the dual wavelength of 440-675 nm, 440-870 nm, and 500-870 nm are used to calculate AOD at 550 nm (τ_{550}). If AOT for 551 nm, 555 nm, 531 nm or 532 nm exist, then these values are directly used as AOD 550 nm. Otherwise, the AOT at wavelength λ_A (less than 550 nm), i.e., τ_A , AOT at wavelength λ_B (larger than 550 nm), i.e., τ_B, and Ångström exponent between wavelengths λ_A and λ_B (α) are used to derive AOD 550 nm using the following equations:

$$\tau_{550} = \tau_A \left(\frac{550}{\lambda_A}\right)^{-\alpha} \quad \text{if } \tau_A \text{ is available ,} \qquad (2)$$

$$\tau_{550} = \tau_B \left(\frac{550}{\lambda_B}\right)^{-\alpha} \quad \text{if } \tau_B \text{ is available.} \quad (3)$$

In a manner similar to the process of screening SDA COD data, monthly AOD 550 nm data with less than three days of records in a given month are removed. When calculating the annual means we excluded years having less than five months of records. Finally, to calculate the climatology of 2003-2015, only stations with at least three years of records during this period are used totaling to 351.

We also developed a method to derive DOD at 550 nm from AOD at 550 nm based on the relationship between Ångström exponent and fine-mode AOD established by Anderson et al. (2005; their Eq. 5). This adds a few more sites over the Sahel than the SDA COD stations. DOD is calculated by subtracting the fine-mode AOD from the total AOD. Due to the large uncertainties of single scattering albedo in AERONET records over regions where AOD is lower than 0.4 (e.g., Dubovik and King, 2000; Holben et al., 2006; Andrews et al., 2017), we did not use single scattering albedo to screen AOD to further separate dust from scattering aerosols. Therefore, the derived AERONET DOD over coastal stations may be contaminated by sea salt.

2) RSMAS surface dust concentration

The Rosenstiel School of Marine and Atmospheric Science (hereafter RSMAS dataset) at University of Miami collected mass concentration of dust, sea salt, and sulfate over stations globally, with most of stations on islands (Savoie and Prospero, 1989). The dataset has been widely used for model evaluation (e.g., Ginoux et al., 2001; Huneeus et al., 2011).

Only stations with records longer than four years were used and of those stations only those years with at least eight months of data are used for calculating climatological annual means. So, totally 16 stations are used. Station names, locations, and record length are listed in Table S1 of the Supplement. We compare the climatology of annual mean surface dust concentration with model output during 2000-2015. Note that since most station records end earlier than 1998, the dataset largely represents the climatology during the 1980s and 1990s. Thus the discrepancies between model output and the RSMAS data include both model biases and the difference in surface dust concentration from the 1980s to the 2000s.

3) IMPROVE surface fine dust concentration

The Interagency Monitoring of Protected Visual Environments (IMPROVE) network has collected near-surface particulate matter 2.5 ($PM_{2.5}$) samples in the U.S. since 1988 (Malm et al., 1994; Hand et al., 2011). IMPROVE stations are located in national parks and wilderness areas, and $PM_{2.5}$ sampling is performed twice weekly (Wednesday and Saturday; Malm et al., 1994) prior to 2000 and every third day afterwards. Fine dust (with aerodynamic diameter less than 2.5 μm) concentration is calculated using the concentrations of aluminum (Al), silicon (Si), calcium (Ca), iron (Fe), and titanium (Ti) by assuming oxide norms associated with predominant soil species (Malm et al., 1994; their Eq. 5). This dataset has been widely used to study variations in surface fine dust in the U.S. (e.g., Hand et al., 2016; Hand et al., 2017, Tong et al., 2017; Pu and Ginoux, 2018a). Here only monthly data with at least 50% of daily data available in a month (i.e., at least 5 records) are used. Since station coverage over the

298 central U.S. increases after 2002 (e.g., Pu and Ginoux, 2018a), monthly station data from
299 2002 to 2015 are used and interpolated to a 0.5° by 0.5° grid using inverse distance
300 weighting interpolation. The gridded data are used to evaluate modeled surface fine dust
301 concentrations.
302
303 4) LISA PM_{10} surface concentration
304 Surface PM_{10} concentration from stations from the Sahelian Dust Transect, which
305 was deployed in 2006 under the framework of African Monsoon Multidisciplinary
306 Analysis International Program (Marticorena et al., 2010), were used to examine the
307 surface dust concentration over the Sahelian region. The data are maintained by
308 Laboratoire Interuniversitaire des Systèmes Atmosphériques (LISA) in the framework of
309 the International Network to study Deposition and Atmospheric composition in Africa
310 (INDAAF; Service National d'Observation de l'Institut National des Sciences de
311 l'Univers, France). Three stations are located within the pathway of Saharan and Sahelian
312 dust plumes moving towards the Atlantic Ocean. Here hourly PM_{10} concentrations from
313 these stations, Banizoumbou (Niger, 13.54° N, 2.66° E), Cinzana (Mali, 13.28° N, 5.93°
314 W), and M'Bour (Senegal, 14.39° N, 16.96° W), from 2006 to 2014 are used. The hourly
315 station data are averaged to obtain daily and monthly mean records to compare with
316 model output.
317
318 **2.1.4 Other data**

Soil depth from the Food and Agriculture Organization of the United Nations (FAO/IIASA/ISRIC/ISS-CAS/JRC, 2009) on a 0.08° by 0.08° resolution is used to examine whether the soil depth is too shallow (i.e., less than 15 cm) for wind erosion.

2.2 Retrieving threshold of wind erosion

The monthly climatological threshold of wind erosion is retrieved by matching the frequency distribution of the MODIS DOD at certain level, namely, DOD_{thresh}, with the frequency distribution of surface 10 m winds from the NCEP1 reanalysis over the period from 2003 to 2015. The process can be summarized by the following steps:

Step1: Since dust is emitted from the dry and sparsely-vegetated surface, the daily DOD data is first masked out to remove the influences of non-erodible factors and unfavorable environmental conditions that are known to prevent dust emission using criteria as follows: daily VSM less than 0.1 cm^3 cm^{-3}; monthly LAI less than 0.3; monthly snow cover less than 0.2% (since snow cover percentage is round-up to integer in MODIS product, this criterion actually requires no snow cover); monthly top-layer soil temperature higher than 273.15 K, i.e., over unfrozen surface; and soil depth thicker than 15 cm. These criteria approximate the most favorable land surface conditions for wind erosion.

Similar criteria have been used in previous studies to detect or confine dust source regions. For instance, Kim et al. (2013) used NDVI less than 0.15, soil depth greater than 10 cm, surface temperature greater than 260 K, and without snow cover to mask topography based dust source function. LAI less than 0.3 has been used as a threshold for dust emission in the Community Land Model (Mahowald et al., 2010; Kok et al., 2014a),

342 while gravimetric soil moisture ranging from 1.01 to 11.2 % depending on soil clay
343 content is recommended to constrain dust emission (Fécan et al., 1999). The uncertainties
344 associated with small variations in the retrieval criteria are further quantified and
345 discussed in section 2.3.

346 Step 2: Masked daily DOD from Step 1 is then interpolated to a 0.5° by 0.5° grid
347 using bilinear interpolation. This is close to the horizontal resolution of the GFDL
348 AM4.0/LM4.0 model used in this study. Then the cumulative frequency distribution of
349 daily DOD from 2003 to 2015 is derived at each grid point for each month.

350 Step 3: Daily maximum surface wind speed is first derived from 6-hourly NCEP1
351 surface winds and then interpolated to a 0.5° by 0.5° grid. Following Ginoux and
352 Deroubaix (2017), we use maximum daily wind speed instead of daily mean wind speed,
353 largely because dust emission only occur when wind speed is strong enough, and the
354 emission magnitude is roughly proportional to the third power of surface wind speed in
355 empirical estimations. The cumulative frequency distribution of daily maximum surface
356 wind from 2003 to 2015 is then calculated at each grid point for each month.

357 Step 4: A minimum value of DOD (i.e., DOD_{thresh}) is used to separate dust events
358 from background dust. The cumulative frequency (in %) of dust events passing this
359 threshold is compared to the cumulative frequency of surface winds. The minimum
360 surface winds with the same frequency correspond to the threshold of wind erosion,
361 $V_{threshold}$ (see a schematic diagram in Figure S1 in the Supplement). This operation is
362 performed for all grid points for each month. Ginoux et al. (2012) used $DOD_{thresh} = 0.2$ to
363 separate dust events from background dust and quantify the FoO of local dust events.
364 Similarly, $DOD_{thresh} = 0.2$ is used here in major dusty regions (North Africa, Middle East,

India, northern China), while for less dusty regions, such as the U.S., South America, South Africa, and Australia, $DOD_{thresh} = 0.02$ is used. The reason to use a lower DOD_{thresh} for less dusty regions is because: i) the overall dust emission in these regions are at least ten times smaller than major dusty regions, such as North Africa (e.g., Huneeus et al., 2011); ii) the frequency distribution of DOD in these regions also peaks at a much lower DOD band (see discussion in section 3.3). We also tested the $DOD_{thresh} = 0.5$ for dusty regions and $DOD_{thresh} = 0.05$ for less dusty regions, and results are discussed in sections 2.3 and 3.1.

Figures 1a-e show the seasonal and annual mean FoO (days when DOD is greater than DOD_{thresh}) using $DOD_{thresh} = 0.2$ or 0.02. The shaded area covers major dust sources, and the pattern is very similar to that obtained by Ginoux et al. (2012; their Fig. 5), although there are some differences, largely due to the masked DOD (i.e., from Step 1) used in this study and a lower threshold in less dusty regions. The higher FoO in North Africa during summer in comparison with other seasons is consistent with the summer peak of the frequency of dust source activation derived from the Meteosat Second Generation (MSG) images (Schepanski et al., 2007; their Fig. 1). The relatively high value of FoO over the northern Sahel to southern Sahara is also consistent with dust emission frequency derived from the Meteosat Second Generation Spinning Enhanced Visible and InfraRed Imager (Evan et al., 2015; their Fig. 1).

Note that the selections of masking criteria in Step 1 and DOD_{thresh} in Step 4 are empirical and can add uncertainties to this method. Also, we approximate dust emission using cumulative frequency of DOD, which may overestimate dust emission in regions where the contribution of transported dust is significant and thus underestimate the

388 $V_{threshold}$ in those regions. These uncertainties are further discussed in the following
389 section.
390
391 **2.3 Sensitivities of $V_{threshold}$ ~~associated with~~to retrieval criteria and the selection of**
392 **reanalysis surface winds**
393 Table 2 shows variations in derived annual mean $V_{threshold}$ averaged in nine dust
394 source regions (see Table 1 for locations) following slight changes of retrieval criteria:
395 soil moisture, LAI, snow coverage, and DOD_{thresh}. When the soil moisture threshold is
396 changed from 0.1 to 0.15 cm^3 cm^{-3} or without the soil moisture constraint, the variations
397 in $V_{threshold}$ are quite small, ranging from 0.01 to about 0.73 m s^{-1} (Table 2). Similarly,
398 changes of LAI criteria from 0.15 to 0.5 m^2 m^{-2} or snow coverage from 0.2% to 10%
399 slightly change $V_{threshold}$ — within 1 m s^{-1} over most regions. On the other hand, $V_{threshold}$
400 is quite sensitive to the selection of the DOD_{thresh}. $V_{threshold}$ would increase about 1 to 3 m
401 s^{-1} if using DOD_{thresh}= 0.5 for dusty regions (0.05 for less dusty regions) instead of
402 DOD_{thresh}= 0.2 (or 0.02). For instance, using DOD_{thresh}=0.5 increases the averaged annual
403 mean $V_{threshold}$ over the Sahara from 4.6 m s^{-1} (using DOD_{thresh}=0.2) to about 7.6 m s^{-1}.
404 As mentioned earlier, dust event frequency can be overestimated in regions with
405 high ratio of transported dust and consequently $V_{threshold}$ would be underestimated. Here
406 we provide a rough estimation about the influence of transported dust on $V_{threshold}$ over
407 North Africa. It is hard to separate local dust emission and transported dust in the column
408 integrated DOD, so we use surface DOD data (sDOD; personal communication with
409 Juliette Paireau), i.e., DOD form surface to about 400 m, to approximate the component
410 of DOD due to local emission. sDOD is derived by using DOD vertical profile from the

411 Cloud-Aerosol Lidar with Orthogonal Polarization (CALIOP; Winker et al., 2004;
412 Winker et al., 2007) to first calculate a ratio of near surface DOD (0~400 m) to total
413 DOD (0~12km) and then multiplying the ratio to daily MODIS Aqua DOD over North
414 Africa from 2003-2014. Using sDOD, $V_{threshold}$ over the Sahel would increase from 3.2 to
415 6.0 m s^{-1}, while over the Sahara, $V_{threshold}$ would increase from 4.6 to 7.7 m s^{-1} (Table 2,
416 last column).

417 How $V_{threshold}$ would change when using surface winds from different reanalyses
418 are examined in Table 3. Surface winds from the ERA-Interim produce higher $V_{threshold}$
419 than the NCEP1 by 0.2 to 2.2 m s^{-1}. Using surface winds from the ERA5 also would
420 increase $V_{threshold}$ by 1 to 1.6 m s^{-1} over North Africa and about 1.5 m s^{-1} over Australia
421 but create smaller differences in other regions.

422 In short, $V_{threshold}$ are less sensitive to small changes in the criteria to define a
423 favorable, dry, and sparsely vegetated land surface condition for wind erosion than the
424 choices of DOD_{thresh} or surface wind speeds from different reanalysis products. Over
425 North Africa, not separating transported dust from total DOD may lead to an
426 underestimation of $V_{threshold}$ up to 3 m s^{-1} based on a rough estimation. However, due to
427 the large uncertainties in quantifying transported dust and the regional converge of sDOD
428 dataset, we chose not to incorporate the results from sDOD to the global $V_{threshold.}$

429

430 **2.4 Simulation design**

431 We will examine if the observation-constrained, spatial and temporal varying
432 $V_{threshold}$ would improve dust simulation in the GFDL AM4.0/LM4.0. The AM4.0/LM4.0
433 is a coupled land-atmosphere model newly developed at GFDL (Zhao et al., 2018a,b). It

uses the recent version of the GFDL Finite-Volume Cubed-Sphere dynamical core (FV^3; Putman and Lin, 2007), which is developed for weather and climate applications with both hydrostatic and non-hydrostatic options. Some substantial updates have been incorporated into the AM4.0, such as an updated version of the model radiation transfer code, an alternate topographic gravity wave drag formulation, a double-plume model representing shallow and deep convection, a "light" chemistry mechanism, and modulation on aerosol wet removal by convection and frozen precipitation (Zhao et al., 2018a,b). Here we used a model version with 33 vertical levels (with model top at 1hPa) and cube-sphere with 192×192 grid boxes per cube face (approximately 50 km grid size).

The aerosol physics is based in large part on that of the GFDL AM3.0 (Donner et al., 2011), but with a simplified chemistry where ozone climatology from AM3.0 simulation (Naik et al., 2013) is prescribed. AM4.0 simulates the mass distribution of five aerosols: sulfate, black carbon, organic carbon, dust, and sea salt. Dust is partitioned into five size bins based on radius: 0.1~1 μm (bin 1), 1~2 μm (bin 2), 2~3 μm (bin 3), 3~6 μm (bin 4), and 6~10 μm (bin 5). The dust emission scheme follows the parameterization of Ginoux et al. (2001), as shown in the following equation:

$$F_p = C \times S \times s_p \times V_{10m}^2 \, (V_{10m} - V_t) \qquad \text{(if } V_{10m} > V_t\text{)}, \qquad (4)$$

where F_p is flux of dust of particle size class p, C is a scaling factor with a unit of μg s^2 m^{-5}, here C is set to 0.75×10^{-9}. S is the source function based on topographic depressions (Ginoux et al., 2001), s_p is fraction of each size class, and V_{10m} is surface 10 m wind speed, and V_t = 6 m s^{-1} is the threshold of wind erosion.

456 Three simulations with prescribed sea surface temperature (SST) and sea ice
457 (Table 4) were conducted from 1999 to 2015, with the first year discarded for spin up.
458 The Atmospheric Model Intercomparison Project (AMIP)-style SST and sea ice data
459 (Taylor et al., 2000) are from the Program for Climate Model Diagnosis and
460 Intercomparison (PCMDI), which combined HadISST (Rayner et al., 2003) from UK Met
461 Office before 1981 and NCEP Optimum Interpolation (OI) v2 SST (Reynolds et al.,
462 2002) afterwards. The surface winds in the simulations are nudged toward the NCEP1
463 reanalysis with a relaxation timescale of 6 hours (Moorthi and Suarez, 1992). Note that
464 the nudged surface winds are actually weaker than the surface wind speed simulated by
465 the standard version of AM4.0/LM4.0 without nudging, so the overall magnitude of dust
466 emission is lower than the standard version. Here we choose not to retune the dust
467 emission scheme but instead test the usage of $V_{threshold}$, which theoretically provides a
468 more physics-based way to improve dust simulation. We also choose to keep the tuning
469 factor C (Eq. 4) the same in all simulations to better examine the effects of implementing
470 the newly developed $V_{threshold}$.

471 In the Control run, the default model setting is used for dust emission, with a
472 prescribed 6 m s^{-1} threshold of wind erosion (cf. Ginoux et al., 2019). In the V_{thresh}12mn
473 simulation, the observation based climatological monthly $V_{threshold}$ is used to replace the
474 constant wind erosion threshold. The default source function S in Eq. 4 only allows dust
475 emission over bare ground by masking out regions with vegetation cover. Since LAI
476 masking is already applied in the retrieval of $V_{threshold}$ (i.e., LAI<0.3), we choose to use a
477 source function that is the same as the default source function S but without vegetation
478 masking, i.e., S' (Figure S2 in the supplement). This allows the influence of the spatial

and temporal variations in $V_{threshold}$ to be fully examined. The combination of source function S' and $V_{threshold}$ also extends dust source from bare ground to sparsely vegetated area as outlined by $V_{threshold}$, e.g., over central North America, central India, and part of Australia, and can increase dust emission in these regions. The pattern of extended dust source area largely resembles the vegetated dust source identified by Ginoux et al. (2012; their Fig. 15b) and Kim et al. (2013; their Fig. 9). All the other settings are the same as the Control run. The V_{thresh}Ann simulation is the same as the V_{thresh}12mn but uses the annual mean $V_{threshold}$ for each month. Since the same SST and sea ice are prescribed for all simulations and land use dose not change much during the short duration of simulation, the differences in simulated dynamic vegetation by LM4.0 among the three simulations are actually very small and can be ignored (see Figures S3-4 in the Supplement).

3. Results

3.1 Thresholds of wind erosion with DOD_{thresh} = 0.2 (or 0.02) and DOD_{thresh} = 0.5 (or 0.05)

Figures 1f-j show the derived threshold of wind erosion for each season and annual mean using DOD_{thresh} =0.2 (or 0.02). The seasonal variations in wind erosion threshold are largely due to the variations in DOD and surface wind frequency distributions that are in turn associated with variations in land surface features, such as soil moisture, soil temperature, snow cover, and vegetation coverage in each month. $V_{threshold}$ is generally lower in MAM and JJA (SON and DJF) for Northern (Southern)

501 Hemisphere dusty regions than in other seasons, consistent with higher FoO in these
502 seasons. $V_{threshold}$ values are also lower in regions with a high FoO (Figs. 1a-e).

503 The distributions of $V_{threshold}$ for annual mean (black bars) and dusty seasons
504 (color lines; MAM and JJA for the Northern Hemisphere and SON and DJF for the
505 Southern Hemisphere) for each dust source region (see Fig. 1f and Table 1 for locations)
506 are shown in Figs. 2a-i. In the Sahel and Sahara, the annual mean $V_{threshold}$ peaks around 4
507 and 4.5-5.5 m s^{-1}, respectively (Figs. 2a-b). This magnitude is lower than indicated from
508 previous studies based on station observations in the region, e.g., Helgren and Prospero
509 (1987) found the threshold velocity over eight stations in Northwest Africa ranged from
510 6.5 to 13 m s^{-1} during summer in 1974. Chomette et al. (1999) and Marsham et al. (2013)
511 also reported higher wind erosion thresholds around 6-9 m s^{-1} at individual stations. On
512 the other hand, Cowie et al. (2014) found that the annual threshold of wind erosion at the
513 25% level, i.e., when surface condition is favorable for dust emission, can be lower than 6
514 m s^{-1} at some sites in the Sahel (their Fig. 5). Several factors may contribute to the
515 discrepancies. Firstly, studies suggest that reanalysis datasets may underestimate surface
516 wind speed in spring and for monsoon days in Africa (e.g., Largeron et al., 2015), and
517 therefore could lead to a lower value of $V_{threshold}$ than that derived from station
518 observations. In fact, Bergametti et al. (2017) found even 3-hourly wind speed record at
519 stations may miss short events with high wind speed. As shown in Table 3, among the
520 reanalysis wind products tested here, the NCEP1 actually produced a lower $V_{threshold}$ in
521 North Africa than the other two reanalyses. Secondly, using DOD frequency to
522 approximate dust emission may lead to an overestimation of dust emission over regions
523 such as the southern Sahel where transported dust is a large component and consequently

524 an underestimation of $V_{threshold}$. Based on our rough estimation, $V_{threshold}$ in North Africa
525 can be underestimated by up to 3 m s^{-1} (section 2.3). In addition, different analysis time
526 periods or methods to retrieve the wind erosion threshold may also contribute to the
527 differences.

528 The annual mean $V_{threshold}$ in Arabian Peninsula is a bit higher, with mean values
529 at 5.2 m s^{-1} (Fig. 2c). The $V_{threshold}$ over northern China is even higher, with an annual
530 mean of 7.8 m s^{-1}. This is consistent with the results of Kurosaki and Mikami (2007),
531 who found that under favorable land surface conditions the threshold wind speed ranges
532 from 4.4± 0.6 m s^{-1} in Taklimakan Desert to 6.9± 1.2 m s^{-1} over the Loess Plateau and
533 around 9.8± 1.6 m s^{-1} in the Gobi Desert. These values are also consistent with Ginoux
534 and Deroubaix (2017) who found that regional mean wind erosion threshold over
535 northern China ranges from 6.5 to 9.1 m s^{-1}. In India, the $V_{threshold}$ peaks at about 4.5 m s^{-1}
536 and 6.5 m s^{-1}, respectively (Fig. 2e). The second peak is probably related to
537 anthropogenic dust sources over the central Indian subcontinent (Ginoux et al., 2012).
538 We also note that in the Northern Hemisphere, the $V_{threshold}$ in dusty seasons is shifted
539 towards lower values than the annual mean (blue and green lines in Figs. 2a-f), but is
540 similar to the annual mean in the Southern Hemisphere (especially South America and
541 Australia), indicating stronger influences of surface variability in the Northern
542 Hemisphere.

543 Fig. 3 shows the seasonal mean and annual mean global $V_{threshold}$ using DOD_{thresh}
544 =0.5 (or 0.05). The corresponding distribution of annual mean $V_{threshold}$ in each region is
545 shown in Figure S5 in the Supplement. The derived $V_{threshold}$ is generally higher than
546 using DOD_{thresh} =0.2 (or 0.02), especially over North Africa, the Arabian Peninsula,

India, and Asia (Fig. 3 and Table 2). The results are thus closer to previous station based studies over North Africa. On the other hand, over northern China, $V_{threshold}$ is around or greater than 8 m s^{-1} (Fig. 3e), slighter higher than previous estimates (e.g., Kurosaki and Mikami 2007; Ginoux and Deroubaix 2017).

In the following section, we will exam if the spatial and temporal varying $V_{threshold}$ would improve model simulation of DOD spatial pattern, seasonal variations, frequency distribution and surface dust concentrations in the GFDL AM4.0/LM4.0. Results using $V_{threshold}$ with DOD_{thresh} =0.2 (or 0.02) are shown in sections 3.2 to 3.3 and results using $V_{threshold}$ with DOD_{thresh} =0.5 (or 0.05) are briefly discussed in section 4.

3.2 $V_{threshold}$ in the GFDL AM4.0/LM4.0 model

In this section we analyze the model output using the default setting (Control; Table 4), 12-month (V_{thresh}12mn), and annual mean $V_{threshold}$ (V_{thresh}Ann) by comparing model results with multiple observational datasets and MODIS DOD.

3.2.1 Climatology of AOD and DOD

In order to compare the model results with observations, we first show the climatology of AERONET AOD and COD from 2003 to 2015. The length of records for each station is shown in Figure S6 in the Supplement. As shown in Figure 4, annual mean global AOD is highest over Africa, the Arabian Peninsula, Indian subcontinent, and Southeast Asia. In the latter two regions, high sulfate concentrations (e.g., Ginoux et al., 2006) and organic carbon from biomass burning in Southeast Asia (e.g., Lin et al., 2014) contribute substantially to the total AOD. The SDA COD shows the optical depth due to

570 coarse aerosols, which includes both dust and sea salt, and sea salt over coastal regions or
571 islands can be a major contributor. Here, high values (>0.2) are largely located over
572 dusty regions such as North Africa, the Arabian Peninsula, and northern India (Fig. 4b).
573 Figures 5a-b show the scatter plots of modeled AOD and COD in the Control run
574 versus AERONET AOD and COD, respectively. Here column-integrated extinction from
575 both dust and sea salt is used to calculated COD in the model. The relative differences
576 (%) between AM4.0 output and AERONET station data are also shown (Figs. 5c-d). The
577 percentage of DOD to total COD in the model is displayed at the bottom (Fig. 5e). The
578 simulated AOD is lower than that from the AERONET over North Africa, the Middle
579 East, and western India, largely due to low values of COD simulated in these regions
580 (Fig. 5d). Besides these regions, the COD over North America, South America, South
581 Africa, and northern Eurasia is also, for the most part, underestimated by the model. Dust
582 is the dominant contributor to the COD value over most of these low COD regions,
583 except over the central to eastern North America and central South America (Fig. 5e).
584 COD (and effectively DOD given its dominance in most regions) was better
585 simulated in the subsequent model run using a prescribed 12-month $V_{threshold}$ in terms of
586 both magnitude and spatial pattern. Figure 6 shows the results from the V_{thresh}12mn
587 simulation. COD is better captured while the AOD effectively moves from a negative to a
588 slightly positive bias (Figs. 6a-d). Most sites over North Africa and the Middle East show
589 a relatively small difference with AERONET COD (Fig. 6d). Over the Indian
590 subcontinent, COD is overestimated, while over North America excluding the east coast,
591 northern Eurasia, and part of South America, COD is also better captured than in the
592 Control run.

These improvements are largely associated with a better simulation of DOD in the "dust belt" (i.e., North Africa and the Middle East). Figure 7 shows the DOD at 550 nm derived from AERONET AOD (see methodology for details) versus that from the V_{thresh}12mn simulation. Over most stations in the Sahel, Mediterranean coasts, and central Middle East, the relative differences between modeled and observed DOD is within ± 25%.

Figure 8 shows the regional averaged annual mean DOD over nine dusty regions from MODIS and three simulations. The Control run largely underestimates DOD in all regions, while the magnitude of DOD is better captured in the V_{thresh}12mn and V_{thresh}Ann simulations, although slightly overestimated in the Sahel and greatly overestimated over Australia. In general, DOD simulated by the V_{thresh}Ann run using a constant annual mean $V_{threshold}$ is higher than that simulated by the V_{thresh}12mn run, consistent with the higher dust emission in the V_{thresh}Ann run (Table S2 in the Supplement). Lack of soil moisture constraint in the model, which is a very important element in capturing the variation of DOD in Australia (Evans et al., 2016), may contribute to the large overestimation of DOD in Australia.

3.2.2 Climatology of surface dust concentration

While DOD is a key parameter associated with the climate impact of dust, surface dust concentration is an important factor affecting local air quality. Here we compare the modeled surface dust concentration with RSMAS station observations. Model output is averaged from 2000 to 2015 to form the annual climatology. Consistent with the DOD output, the Control run largely underestimates surface dust concentrations at almost all of

616 the sites (except sites 9 and 15; Figure 9 top panel). The underestimation is reduced in the
617 V_{thresh}Ann simulation (Fig. 9, middle panel), with seven stations having
618 model/observation ratios between 0.5 and 2 (white triangles). Over the coastal U.S. (e.g.,
619 sites 16 and 13), dust concentrations are overestimated, consistent with the
620 overestimation of DOD over the U.S. and the Sahel (Fig. 8). Dust concentrations in
621 Australia and the east coast of China are also overestimated by more than five-folds.
622 Surface dust concentration is further improved in the V_{thresh}12mn simulation (Fig. 9,
623 bottom), with eight stations showing a model/observation ratio between 0.5 and 2 and
624 only four stations overestimating or underestimating dust concentrations by more than
625 five times.

626 Simulated surface fine dust concentration (calculated as dust bin 1+0.25×dust bin
627 2) in the U.S. is compared with gridded IMPROVE data (Figure 10). While the Control
628 run largely underestimates surface fine dust concentration, the simulated concentration is
629 overall too high in the V_{thresh}Ann run. The spatial pattern of fine dust concentration is
630 better captured in the V_{thresh}12mn run, with higher values over the southwestern U.S., but
631 the magnitude is still overestimated, and additional dust hot spots are simulated over the
632 northern Great plains and the Midwest, which are not shown in the IMPROVE data. Such
633 an overall overestimation may be attributed to lack of soil moisture modulation in the
634 dust emission scheme. The way in which dust bins are partitioned in the model can add
635 uncertainties to model's representation of surface fine dust concentrations as well. On
636 the other hand, the relatively low spatial coverage of IMPROVE sites over the northern
637 Great Plains and Midwest (e.g., Pu and Ginoux, 2018a) may also add uncertainties to the
638 data itself.

639 **3.2.3 Seasonal cycles**

640 Figure 11 compares the seasonal cycle of DOD from three simulations with
641 MODIS DOD in nine dusty regions. The seasonal cycle of gridded AERONET COD (as
642 an approximation to DOD; on a 0.5° by 0.5° grid) is also shown. Since the gridded COD
643 may have large uncertainties over regions with only a few stations, such as the Sahel,
644 Sahara, northern China, and South Africa, MODIS DOD is used as the main reference in
645 the comparison. Seasonal cycles are better captured by the V_{thresh}12mn simulation in the
646 Sahel, the Sahara, and the Arabian Peninsula (Figs. 11a-c), although the spring and
647 summer peak in the Sahel is overestimated and winter minimum in the Sahara is
648 underestimated. The MAM peak of MODIS DOD in northern China is missed by both
649 V_{thresh}12mn and V_{thresh}Ann simulations (Fig. 11d), while the JJA peak over India is
650 largely overestimated (Fig. 11e). Over the U.S. dusty region, the seasonal cycle in the
651 V_{thresh}12mn simulation is slightly underestimated compared to MODIS DOD but
652 overestimated from May to August in the V_{thresh}Ann simulation (Fig. 11f). DOD is
653 underestimated in South Africa in all three simulations (Fig. 11g). Over South America,
654 the peak from October to February is roughly captured by the V_{thresh}12mn run but is
655 overestimated by the V_{thresh}Ann run (Fig. 11h). The seasonal cycles of DOD in Australia
656 are very similar in all three simulations and largely resemble that in the MODIS, although
657 both the V_{thresh}12mn and V_{thresh}Ann simulations overestimate the DOD by about an order
658 of magnitude.

659 Figure 12 shows the seasonal cycle of COD from 12 AERONET SDA sites over
660 North Africa and nearby islands (see Figure S7 in the Supplement for site locations)
661 along with MODIS DOD and DOD simulated in three runs. The magnitude of

662 AERONET COD and MODIS DOD in these sites are very similar, despite missing values
663 at sites 1, 4, 5, 8, 11, and a smaller value at site 2 in MODIS. Over most of the sites, the
664 seasonal cycle is better captured in the V_{thresh}12mn and V_{thresh}Ann simulations than the
665 Control run, although the peak over Cairo_EMA_2 (site 12) is slightly underestimated,
666 which is consistent with the underestimation of annual mean DOD in the area (Fig. 7).
667 We also examined the seasonal cycle of PM_{10} surface concentration at three
668 Sahelian INDAAF stations (see Figure S7 in the Supplement for site locations) from the
669 LISA project. Figures 13a-c show PM_{10} surface dust concentration (here dust dominates
670 total PM_{10} concentration) from the Control, V_{thresh}12mn, and V_{thresh}Ann simulations
671 versus observed PM_{10} concentration from three LISA sites. PM_{10} concentrations in these
672 sites peak during boreal winter and spring and reach minima from July to September.
673 These seasonal variations are associated with the dry northerly Harmattan wind in boreal
674 winter and spring that transports Saharan dust southward to the Guinean coast and the
675 scavenging effect of monsoonal rainfall in boreal summer that removes surface dust
676 (Marticorena et al., 2010; Fiedler et al., 2015). While the Control run does not capture the
677 seasonal cycles in these sites, the V_{thresh}12mn run largely captures the spring peak and
678 summer minimum, although the magnitude is overestimated. In all three sites, the
679 simulated concentration in the V_{thresh}Ann run is larger than that in the V_{thresh}12mn run,
680 especially in boreal fall to early spring. Such an overestimation is probably due to the
681 prescribed constant annual mean $V_{threshold}$, which is lower than it would be during the less
682 dusty season (i.e., boreal fall to winter) and thus increases dust emission and surface
683 concentration.

Figs. 13d-f show the seasonal cycle of DOD from three AERONET sites co-located with LISA INDAAF stations and from three simulations. The V_{thresh}12mn and V_{thresh}Ann simulations largely captured the seasonal cycle of DOD at these sites. The overestimation of near surface PM_{10} dust concentration (Figs. 13a-c) and the generally well-captured column integrated DOD (Figs. 13d-f) indicate that model likely underestimates dust concentration in the atmospheric column above the surface, which needs further investigation in future studies.

3.2.4 A dust storm over U.S. northern Great Plains on October 18th, 2012

Can the AM4.0/LM4.0 with prescribed $V_{threshold}$ better represent individual dust events? Here we examine a major dust storm captured by MODIS Aqua true color-image on Oct. 18th, 2012 (https://earthobservatory.nasa.gov/images/79459/dust-storm-in-the-great-plains) over the U.S. northern Great Plains. There was a severe drought in 2012 with anomalously low precipitation centered over the central U.S. (e.g., Hoerling et al., 2014). The dry conditions favored dust storm development when there were intensified surface winds. However, this storm was not predicted by the forecast models, such as the Goddard Earth Observing System version 5 (GEOS-5; Rienecker et al., 2008) and Navy Aerosol Analysis Prediction System (NAAPS; Witek et al., 2007; Reid et al., 2009; Westphal et al., 2009).

As shown in Figure 14, MODIS DOD ~~also~~ captures this event, with a peak value above 0.5 over southwest Nebraska and northern Kansas on Oct. 18th, 2012. The V_{thresh}12mn run also largely captures this event (Fig. 14 bottom panel), although the Control run totally misses it (not shown). In the model, the dust storm appears in South

Dakota and Nebraska on Oct. 17th, 2012, along with the anomalous southwesterly winds. It reaches a maximum on Oct. 18th, in association with intensified anomalous southwesterly winds at the surface and an anomalous low-pressure system at 850 hPa (Figure S8 in the Supplement). Note that the modeled dust storm center is located a bit northeastward compared to the MODIS DOD pattern and it also has greater magnitude and covers a larger area. On Oct. 19th, both the anomalous low-pressure system and surface wind speeds weaken and the dust storm dissipates, with slightly elevated DOD levels over a region extending over the lower Mississippi River basin and the Midwest. This is somewhat consistent with MODIS records, which also shows slightly higher DOD levels over Tennessee and northern Alabama on Oct. 19th, regardless of large area of missing values.

3.3 Frequency distribution of DOD in the model versus that from MODIS

Figure 15 shows the frequency distribution of regional mean DOD during one dusty season (MAM in the Northern Hemisphere and SON in the Southern Hemisphere) for nine regions. Results from MODIS, the Control, and V_{thresh}12mn runs are shown in black, blue, and orange lines, respectively. In most dusty regions, such as the Sahara, Sahel, Arabian Peninsula, India, and northern China, MODIS DOD frequency largely peaks between 0.2 to 0.4, while DOD frequency peaks at a much lower level between 0.02 to 0.08 in less dusty regions, such as the U.S., South America, South Africa and Australia. This also justifies our selection of DOD_{thresh} of 0.02 (instead of 0.2) in the less dusty regions. The DOD distribution in the Control run is biased low and peaks around 0.05 in those dusty regions and between 0 and 0.01 in less dusty regions. The frequency

730 is much better captured in the V_{thresh}12mn run over the Arabian Peninsula and the Sahel,
731 slightly improved but still biased low over the Sahara, northern China, India, and the U.S.
732 The modeled frequency in the V_{thresh}12mn run is biased high in Australia (peaks outside
733 the maximum of x-axis, not shown) and shows little improvement over South Africa and
734 South America. The overall improvement of DOD frequency using the time-varying 2D
735 $V_{threshold}$ occurs mostly over major dusty regions, which is consistent with the
736 improvements in DOD climatology and seasonal cycle in the model simulations.
737
738 **4. Discussion**
739 A global distribution of the threshold of wind erosion is retrieved using high
740 resolution MODIS DOD and land surface constraints from relatively high–resolution
741 satellite products and reanalyses. While this climatological monthly $V_{threshold}$ provides
742 useful information about the spatial and temporal variations in wind erosion threshold,
743 there are some uncertainties associated with it. Here DOD frequency is derived using
744 MODIS and other satellite products, thus the uncertainties in the satellite products are
745 inherited in the derived DOD frequency distribution. Due to the cloud screening
746 processes of MODIS products, dust activities over cloud-covered regions may be
747 underestimated. Also, DOD frequency is derived based on daily observations over a 13-
748 year record, so that some variability of dust emission associated with alluvial sediments
749 deposited by seasonal flooding may be not captured. Diurnal variability of dust emission
750 and short-duration events such as haboobs are also not included. Since DOD is a column
751 integrated variable, it includes both local emitted and remotely transported dust. When
752 using DOD frequency distribution to approximate dust emission, it may overestimate dust

753 emission in regions where transported dust is dominated and lead to an underestimation
754 of $V_{threshold}$. Future studies to better quantify the influences of transported dust would
755 further improve quantitative retrieval of $V_{threshold,}$

756 Previous study found that over regions such as North Africa, reanalysis products
757 may underestimate surface wind speed in spring and monsoon seasons but overestimate it
758 during dry nights (e.g., Largeron et al., 2015). This is largely because mechanisms such
759 as density current that can enhance surface wind speed are not parameterized in the
760 atmospheric models to produce the reanalysis products, while coarse spatial and temporal
761 sampling may also contribute to the underestimation of reanalysis wind speeds. The
762 selection of surface winds from different reanalysis products also affects the derived
763 $V_{threshold.}$ Among the three reanalyses examined here, $V_{threshold,}$ derived from the NCEP1
764 reanalysis shows slightly lower values than others.

765 In addition, $V_{threshold}$ is derived by matching the frequency distribution of DOD at
766 certain levels (i.e., DOD_{thresh}) with the frequency distribution of daily maximum wind.
767 An issue is that selecting a value of DOD_{thresh} is quite empirical. The influences of soil
768 properties such as soil cohesion, particle size, and particle compositions on the threshold
769 of wind erosion (e.g., Fécan et al., 1999; Alfaro and Gomes, 2001; Shao, 2001; Kok et
770 al., 2014b) are not explicitly examined here and will need further investigation.

771 The influences of $V_{threshold}$ on AM4.0/LM4.0 results are twofold. On the one hand,
772 it modifies the default constant threshold of wind erosion (V_t in Eq. 4) by allowing spatial
773 and temporal variations of wind erosion threshold over bare ground, i.e., within the
774 domain of default dust source function S (Figs. S9a-e in the Supplement). On the other
775 hand, it slightly extends the potential emission area to sparsely-vegetated regions as

outlined by $V_{threshold}$ (Figs. S9f-j in the Supplement). Which effect dominates? Taking the V_{thresh}12mn simulation as an example, Figure S10 shows the differences of dust emission with the Control run. The increase of dust emission in the V_{thresh}12mn simulation (also summarized in Table S2 in the Supplement) is largely associated with the enhanced emission over the bare ground (Figs. S10a-e in the Supplement), mainly over the regions with reduced wind erosion threshold (Figs. S9a-e in the Supplement). The increased emission over sparsely-vegetated area over regions such as the southern Sahel, India, and Australia plays a minor role. This is consistent with Kim et al. (2013), who found global dust emission in the Georgia Institute of Technology–Goddard Ozone Chemistry Aerosol Radiation and Transport (GOCART) model is dominated by emission from bare ground.

The major benefit of using the spatial and temporal varying $V_{threshold}$ is that it improves the simulation of DOD spatial pattern (Figs. 6-7), seasonal cycle (Figs. 11-13), and frequency distribution (Fig. 15) as well as the spatial pattern of surface dust concentrations (Figs. 9-10), which cannot be achieved by simply modifying the global tuning factor (i.e., C in Eq. 4) to fit the observations such as surface concentrations or optical depth.

The default setting in the Control run produced a relatively low global dust emission (978 Tg yr^{-1}) in comparison with the AeroCom multi-model median (1123 Tg yr^{-1}; Huneeus et al. 2011) or a previous estimation based on MODIS DOD (1223 Tg yr^{-1}; Ginoux et al. 2012). So we also conducted a test run (Control II) to increase global dust emission in the Control run to about 1232 Tg yr^{-1} by enlarging C in Eq. 4. The magnitude of DOD slightly increases, e.g., over the Sahel annual mean increases from 0.07 to 0.09,

798 however, there's no improvement in terms of seasonal cycle or spatial pattern, as
799 expected.

800 We also examined the performance of $V_{threshold}$ using DOD_{thresh}= 0.5 (or 0.05) in
801 the AM4.0/LM4.0. Similarly, we conducted simulations with 12-month $V_{threshold}$
802 (V_{thresh}12mn II) and annual mean $V_{threshold}$ (V_{thresh}Ann II), all using the same tuning factor
803 as in the Control II. We found similar improvement in DOD seasonal cycle and weaker
804 improvement in DOD spatial pattern and frequency distribution and surface dust
805 concentrations (except with the IMPROVE data over the U.S. and surface concentrations
806 over the Sahel, where dust concentrations are previously overestimated). This is largely
807 because higher $V_{threshold}$ leads to lower global dust emissions in the V_{thresh}Ann II (1961
808 Tg yr^{-1}) and V_{thresh}12mn II simulations (1705 Tg yr^{-1}) and overall lower DOD. Over
809 Mediterranean coast, Europe, and northern Asia, DOD spatial pattern is not as well
810 captured in the V_{thresh}12mn II run as in the V_{thresh}12mn run, likely due to relatively high
811 $V_{threshold}$ in these regions.
812

813 **5. Conclusion**

814 While dust aerosols play important roles in the Earth's climate system, large
815 uncertainties exist in modeling its lifecycle (e.g., Huneeus et al., 2011; Pu and Ginoux,
816 2018b). Constant thresholds of wind erosion are widely used in climate models for
817 simplicity. Here, high-resolution MODIS Deep Blue dust optical depth (DOD) and
818 surface wind speeds from the NCEP1 reanalysis, along with other land surface factors
819 that affect wind erosion, such as soil moisture, vegetation cover, snow cover, soil
820 temperature, and soil depth, were used to develop a time-varying two-dimensional

climatological threshold of wind erosion, $V_{threshold}$, based on the seasonal variations of DOD and surface wind distribution frequencies. $V_{threshold}$ is generally lower in dusty seasons, i.e., MAM and JJA (SON and DJF) in the Northern (Southern) Hemisphere.

The climatological monthly $V_{threshold}$ was then incorporated into the GFDL AM4.0/LM4.0 model to examine the potential benefits relative to the use of a constant threshold. In comparison with the simulation using the default setting of a globally constant threshold of wind erosion (6 m s^{-1}), both the magnitude of DOD and surface dust concentrations are increased and closer to observations. However, different from modifying the global tuning factor (i.e., C in Eq. 4) to increase the overall magnitudes of DOD or surface dust concentrations, we found the spatial and temporal varying $V_{threshold}$ largely improves the simulation of the spatial pattern, seasonal cycle, and frequency distribution of DOD over Northern Hemisphere dusty regions, such as North Africa and the Arabian Peninsula, and slightly improvesd over India, the western to central U.S., and northern China. The seasonal cycle of DOD are also slightly improved in South America, although change little in South Africa. The incorporation of $V_{threshold}$ leads to an overestimation of DOD in Australia, likely in association with the absence of soil moisture constraints on dust emission in the model.

The spatial pattern of surface dust concentrations is also improved when spatial and temporal varying ~~time-varying~~ $V_{threshold}$ is incorporated. The fine dust concentration in the U.S. is also better captured, with the maximum of annual mean largely located over the southwestern U.S., although the magnitude is overestimated.

A constant annual mean $V_{threshold}$ is also tested in the model, and is found to overestimate DOD over dusty seasons in the Arabian Peninsula, U.S., India, Australia,

and South America. Surface PM_{10} concentrations in the Sahel during boreal fall and winter seasons are also largely overestimated with this setting. The results indicate the importance of including the seasonal cycle of $V_{threshold}$ in the model. Using time-varying 2D $V_{threshold}$, the model was also able to capture a strong dust storm in the U.S. Great Plains in October 2012, which created deadly accidents, while some dust forecasting models failed to reproduce it.

Finally, this method to retrieve global threshold of wind erosion can be conducted under different resolutions or surface wind reanalsyses or being applied to surface ~~fiction~~ friction velocity datasets to match the resolution/scheme of dust models and may help improve their simulations and forecasting of dust distribution. As discussed in section 4, there are uncertainties associated with this method, and future studies to better quantify the influence of transported dust to overall DOD frequency distribution and incorporating station based surface wind records into the retrieval process will further improve the dataset.

Data availability. Both the monthly and annual mean $V_{threshold}$ data at a 0.5° by 0.5° resolution in NetCDF format is archived at: https://www.gfdl.noaa.gov/pag-homepage/

Author contributions. PG and BP conceived the study. PG processed the MODIS Deep Blue aerosol data and guided model simulations. HG, SM, VN, ES, and MZ assisted with model configurations, while CH, JK, BM, NO, CG, and JP provided guidance on data usage and analysis. BP conducted model simulations, analyzed data and model results, and wrote the paper with contributions from all other co-authors.

Acknowledgements.

This research is supported by NOAA and Princeton University's Cooperative Institute for Climate Science and NASA under grant NNH14ZDA001N-ACMAP and NNH16ZDA001N-MAP. The authors thank Drs. Veronica Chan and Hyeyum Shin for their helpful comments on the early version of this paper and Dr. Sophie Vandenbussche for her valuable suggestions. The helpful comments from two anonymous reviewers and the co-editor improved the paper. We also thank the AERONET program for establishing and maintaining the sunphotometer sites used in this study and the IMPROVE network for the data. IMPROVE is a collaborative association of state, tribal, and federal agencies and international partners. The US Environmental Protection Agency is the primary funding source, with contracting and research support from the National Park Service. The Air Quality Group at the University of California, Davis is the central analytical

887 laboratory, with ion analysis provided by Research Triangle Institute, and carbon analysis
888 provided by Desert Research Institute.
889 The AERONET aerosol optical depth data and SDA data are downloaded from
890 https://aeronet.gsfc.nasa.gov/new_web/download_all_v3_aod.html (last access: June
891 2018; Holben et al. 1998). IMPROVE fine dust data are downloaded from
892 http://views.cira.colostate.edu/fed/DataWizard/ (last access: March 2017, Malm et al.,
893 1994; Hand et al., 2011). MODIS LAI data may be requested by contacting Dr. Ranga
894 Myneni at Boston University.
895
896
897
898
899
900
901
902
903
904
905
906
907
908
909

910 Reference
911
912 Alfaro, S. C., and Gomes, L.: Modeling mineral aerosol production by wind erosion:
913 Emission intensities and aerosol size distributions in source areas, J Geophys Res-
914 Atmos, 106, 18075-18084, Doi 10.1029/2000jd900339, 2001.
915 Anderson, T. L., Wu, Y. H., Chu, D. A., Schmid, B., Redemann, J., and Dubovik, O.:
916 Testing the MODIS satellite retrieval of aerosol fine-mode fraction, J Geophys
917 Res-Atmos, 110, 10.1029/2005jd005978, 2005.
918 Andrews, E., Ogren, J. A., Kinne, S., and Samset, B.: Comparison of AOD, AAOD and
919 column single scattering albedo from AERONET retrievals and in situ profiling
920 measurements, Atmos Chem Phys, 17, 6041-6072, 10.5194/acp-17-6041-2017,
921 2017.
922 Baddock, M. C., Ginoux, P., Bullard, J. E., and Gill, T. E.: Do MODIS-defined dust
923 sources have a geomorphological signature?, Geophys Res Lett, 43, 2606-2613,
924 10.1002/2015gl067327, 2016.
925 Bangert, M., Nenes, A., Vogel, B., Vogel, H., Barahona, D., Karydis, V. A., Kumar, P.,
926 Kottmeier, C., and Blahak, U.: Saharan dust event impacts on cloud formation
927 and radiation over Western Europe, Atmos Chem Phys, 12, 4045-4063,
928 10.5194/acp-12-4045-2012, 2012.
929 Barchyn, T. E., and Hugenholtz, C. H.: Comparison of four methods to calculate aeolian
930 sediment transport threshold from field data: Implications for transport prediction
931 and discussion of method evolution, Geomorphology, 129, 190-203,
932 10.1016/j.geomorph.2011.01.022, 2011.

933 Bentsen, M., Bethke, I., Debernard, J. B., Iversen, T., Kirkevag, A., Seland, O., Drange,
934 H., Roelandt, C., Seierstad, I. A., Hoose, C., and Kristjansson, J. E.: The
935 Norwegian Earth System Model, NorESM1-M - Part 1: Description and basic
936 evaluation of the physical climate, Geosci Model Dev, 6, 687-720, 10.5194/gmd-
937 6-687-2013, 2013.
938 Bristow, C. S., Hudson-Edwards, K. A., and Chappell, A.: Fertilizing the Amazon and
939 equatorial Atlantic with West African dust, Geophys Res Lett, 37,
940 10.1029/2010gl043486, 2010.
941 Cheng, T., Peng, Y., Feichter, J., and Tegen, I.: An improvement on the dust emission
942 scheme in the global aerosol-climate model ECHAM5-HAM, Atmos Chem Phys,
943 8, 1105-1117, DOI 10.5194/acp-8-1105-2008, 2008.
944 Chomette, O., Legrand, M., and Marticorena, B.: Determination of the wind speed
945 threshold for the emission of desert dust using satellite remote sensing in the
946 thermal infrared, J Geophys Res-Atmos, 104, 31207-31215, Doi
947 10.1029/1999jd900756, 1999.
948 Collins, W. J., Bellouin, N., Doutriaux-Boucher, M., Gedney, N., Halloran, P., Hinton,
949 T., Hughes, J., Jones, C. D., Joshi, M., Liddicoat, S., Martin, G., O'Connor, F.,
950 Rae, J., Senior, C., Sitch, S., Totterdell, I., Wiltshire, A., and Woodward, S.:
951 Development and evaluation of an Earth-System model-HadGEM2, Geosci
952 Model Dev, 4, 1051-1075, 10.5194/gmd-4-1051-2011, 2011.
953 Cook, B. I., Miller, R. L., and Seager, R.: Dust and sea surface temperature forcing of the
954 1930s "Dust Bowl" drought, Geophys Res Lett, 35, 10.1029/2008gl033486, 2008.

955 Cook, B. I., Miller, R. L., and Seager, R.: Amplification of the North American "Dust
956 Bowl" drought through human-induced land degradation, P Natl Acad Sci USA,
957 106, 4997-5001, 10.1073/pnas.0810200106, 2009.
958 Cook, B. I., Seager, R., Miller, R. L., and Mason, J. A.: Intensification of North
959 American Megadroughts through Surface and Dust Aerosol Forcing, J Climate,
960 26, 4414-4430, 10.1175/Jcli-D-12-00022.1, 2013.
961 Cowie, S. M., Knippertz, P., and Marsham, J. H.: A climatology of dust emission events
962 from northern Africa using long-term surface observations, Atmos Chem Phys,
963 14, 8579-8597, 10.5194/acp-14-8579-2014, 2014.
964 Dee, D. P., Uppala, S. M., Simmons, A. J., Berrisford, P., Poli, P., Kobayashi, S., Andrae,
965 U., Balmaseda, M. A., Balsamo, G., Bauer, P., Bechtold, P., Beljaars, A. C. M.,
966 van de Berg, L., Bidlot, J., Bormann, N., Delsol, C., Dragani, R., Fuentes, M.,
967 Geer, A. J., Haimberger, L., Healy, S. B., Hersbach, H., Holm, E. V., Isaksen, L.,
968 Kallberg, P., Kohler, M., Matricardi, M., McNally, A. P., Monge-Sanz, B. M.,
969 Morcrette, J. J., Park, B. K., Peubey, C., de Rosnay, P., Tavolato, C., Thepaut, J.
970 N., and Vitart, F.: The ERA-Interim reanalysis: configuration and performance of
971 the data assimilation system, Q J Roy Meteor Soc, 137, 553-597, 10.1002/qj.828,
972 2011.
973 Donner, L. J., Wyman, B. L., Hemler, R. S., Horowitz, L. W., Ming, Y., Zhao, M., Golaz,
974 J. C., Ginoux, P., Lin, S. J., Schwarzkopf, M. D., Austin, J., Alaka, G., Cooke, W.
975 F., Delworth, T. L., Freidenreich, S. M., Gordon, C. T., Griffies, S. M., Held, I.
976 M., Hurlin, W. J., Klein, S. A., Knutson, T. R., Langenhorst, A. R., Lee, H. C.,
977 Lin, Y. L., Magi, B. I., Malyshev, S. L., Milly, P. C. D., Naik, V., Nath, M. J.,

978 Pincus, R., Ploshay, J. J., Ramaswamy, V., Seman, C. J., Shevliakova, E., Sirutis,
979 J. J., Stern, W. F., Stouffer, R. J., Wilson, R. J., Winton, M., Wittenberg, A. T.,
980 and Zeng, F. R.: The Dynamical Core, Physical Parameterizations, and Basic
981 Simulation Characteristics of the Atmospheric Component AM3 of the GFDL
982 Global Coupled Model CM3, J Climate, 24, 3484-3519, 10.1175/2011jcli3955.1,
983 2011.
984 Draxier, R. R., and Hess, G. D.: An overview of the HYSPLIT_4 modelling system for
985 trajectories, dispersion and deposition, Aust Meteorol Mag, 47, 295-308, 1998.
986 Draxler, R. R., Ginoux, P., and Stein, A. F.: An empirically derived emission algorithm
987 for wind-blown dust, J Geophys Res-Atmos, 115, 10.1029/2009jd013167, 2010.
988 Du, J., Jones, L. A., and Kimball, J. S.: Daily Global Land Parameters Derived from
989 AMSR-E and AMSR2, Version 2, https://doi.org/10.5067/RF8WPYOPJKL2,
990 2017a.
991 Du, J. Y., Kimball, J. S., Jones, L. A., Kim, Y., Glassy, J., and Watts, J. D.: A global
992 satellite environmental data record derived from AMSR-E and AMSR2
993 microwave Earth observations, Earth Syst Sci Data, 9, 791-808, 10.5194/essd-9-
994 791-2017, 2017b.
995 Dubovik, O., and King, M. D.: A flexible inversion algorithm for retrieval of aerosol
996 optical properties from Sun and sky radiance measurements, J Geophys Res-
997 Atmos, 105, 20673-20696, Doi 10.1029/2000jd900282, 2000.
998 Dumont, M., Brun, E., Picard, G., Michou, M., Libois, Q., Petit, J. R., Geyer, M., Morin,
999 S., and Josse, B.: Contribution of light-absorbing impurities in snow to

1000 Greenland's darkening since 2009, Nat Geosci, 7, 509-512, 10.1038/Ngeo2180,
1001 2014.
1002 Dunion, J. P., and Velden, C. S.: The impact of the Saharan air layer on Atlantic tropical
1003 cyclone activity, B Am Meteorol Soc, 85, 353-+, 10.1175/Bams-85-3-353, 2004.
1004 Eck, T. F., Holben, B. N., Reid, J. S., Dubovik, O., Smirnov, A., O'Neill, N. T., Slutsker,
1005 I., and Kinne, S.: Wavelength dependence of the optical depth of biomass
1006 burning, urban, and desert dust aerosols, J Geophys Res-Atmos, 104, 31333-
1007 31349, Doi 10.1029/1999jd900923, 1999.
1008 Evan, A. T., Dunion, J., Foley, J. A., Heidinger, A. K., and Velden, C. S.: New evidence
1009 for a relationship between Atlantic tropical cyclone activity and African dust
1010 outbreaks, Geophys Res Lett, 33, 10.1029/2006gl026408, 2006.
1011 Evan, A. T., Fiedler, S., Zhao, C., Menut, L., Schepanski, K., Flamant, C., and Doherty,
1012 O.: Derivation of an observation-based map of North African dust emission,
1013 Aeolian Res, 16, 153-162, 10.1016/j.aeolia.2015.01.001, 2015.
1014 Evans, S., Ginoux, P., Malyshev, S., and Shevliakova, E.: Climate-vegetation interaction
1015 and amplification of Australian dust variability, Geophys Res Lett, 43, 11823-
1016 11830, 10.1002/2016gl071016, 2016.
1017 Fécan, F., Marticorena, B., and Bergametti, G.: Parametrization of the increase of the
1018 aeolian erosion threshold wind friction velocity due to soil moisture for arid and
1019 semi-arid areas, Ann Geophys-Atm Hydr, 17, 149-157, DOI
1020 10.1007/s005850050744, 1999.

1021 Fiedler, S., Kaplan, M. L., and Knippertz, P.: The importance of Harmattan surges for the
1022 emission of North African dust aerosol, Geophys Res Lett, 42, 9495-9504,
1023 10.1002/2015gl065925, 2015.
1024 Fung, I. Y., Meyn, S. K., Tegen, I., Doney, S. C., John, J. G., and Bishop, J. K. B.: Iron
1025 supply and demand in the upper ocean, Global Biogeochem Cy, 14, 281-295, Doi
1026 10.1029/1999gb900059, 2000.
1027 Garrigues, S., Lacaze, R., Baret, F., Morisette, J. T., Weiss, M., Nickeson, J. E.,
1028 Fernandes, R., Plummer, S., Shabanov, N. V., Myneni, R. B., Knyazikhin, Y., and
1029 Yang, W.: Validation and intercomparison of global Leaf Area Index products
1030 derived from remote sensing data, J Geophys Res-Biogeo, 113,
1031 10.1029/2007jg000635, 2008.
1032 Gillette, D. A., Adams, J., Endo, A., Smith, D., and Kihl, R.: Threshold Velocities for
1033 Input of Soil Particles into the Air by Desert Soils, J Geophys Res-Oceans, 85,
1034 5621-5630, 10.1029/JC085iC10p05621, 1980.
1035 Gillette, D. A., and Passi, R.: Modeling Dust Emission Caused by Wind Erosion, J
1036 Geophys Res-Atmos, 93, 14233-14242, DOI 10.1029/JD093iD11p14233, 1988.
1037 Ginoux, P., Chin, M., Tegen, I., Prospero, J. M., Holben, B., Dubovik, O., and Lin, S. J.:
1038 Sources and distributions of dust aerosols simulated with the GOCART model, J
1039 Geophys Res-Atmos, 106, 20255-20273, Doi 10.1029/2000jd000053, 2001.
1040 Ginoux, P., Horowitz, L. W., Ramaswamy, V., Geogdzhayev, I. V., Holben, B. N.,
1041 Stenchikov, G., and Tie, X.: Evaluation of aerosol distribution and optical depth
1042 in the Geophysical Fluid Dynamics Laboratory coupled model CM2.1 for present
1043 climate, J Geophys Res-Atmos, 111, 10.1029/2005jd006707, 2006.

1044 Ginoux, P., Garbuzov, D., and Hsu, N. C.: Identification of anthropogenic and natural
1045 dust sources using Moderate Resolution Imaging Spectroradiometer (MODIS)
1046 Deep Blue level 2 data, J Geophys Res-Atmos, 115, 10.1029/2009jd012398,
1047 2010.
1048 Ginoux, P., Prospero, J. M., Gill, T. E., Hsu, N. C., and Zhao, M.: Global-Scale
1049 Attribution of Anthropogenic and Natural Dust Sources and Their Emission Rates
1050 Based on MODIS Deep Blue Aerosol Products, Rev Geophys, 50,
1051 10.1029/2012rg000388, 2012.
1052 Ginoux, P., and Deroubaix, A.: Space observations of dust in East Asia, Air pollution in
1053 Eastern Asia: an integrated perspective, edited by: Bouarar, I., Wang, X., and
1054 Brasseur, G. P., Springer, 2017.
1055 Ginoux, P., Malyshev, S., Shevliakova, E., Chan, H. G., Guo, H., Milly, C., Naik, V.,
1056 Pascale, S., Paulot, F., Pu, B., Zhao, M., and Kapnick, S.: Distribution of
1057 absorbing aerosols in snow over high mountain ranges in GFDL AM4/LM4, in
1058 preparation, 2019.
1059 Hand, J. L., Copeland, S. A., Day, D. E., Dillner, A. M., Indresand, H., Malm, W. C.,
1060 McDade, C. E., Moore, C. T., Pitchford, M. L., Schichtel, B. A., and Watson, J.
1061 G.: IMPROVE (Interagency Monitoring of Protected Visual Environments):
1062 Spatial and seasonal patterns and temporal variability of haze and its constituents
1063 in the United States, 2011.
1064 Hand, J. L., White, W. H., Gebhart, K. A., Hyslop, N. P., Gill, T. E., and Schichtel, B. A.:
1065 Earlier onset of the spring fine dust season in the southwestern United States,
1066 Geophys Res Lett, 43, 4001-4009, 10.1002/2016gl068519, 2016.

1067 Hand, J. L., Gill, T. E., and Schichtel, B. A.: Spatial and seasonal variability in fine
1068 mineral dust and coarse aerosol mass at remote sites across the United States, J
1069 Geophys Res-Atmos, 122, 3080-3097, 10.1002/2016jd026290, 2017.
1070 Helgren, D. M., and Prospero, J. M.: Wind Velocities Associated with Dust Deflation
1071 Events in the Western Sahara, J Clim Appl Meteorol, 26, 1147-1151, Doi
1072 10.1175/1520-0450(1987)026<1147:Wvawdd>2.0.Co;2, 1987.
1073 Hersbach, H., and Dee, D.: ERA5 reanalysis is in production, ECMWF Newsletter, No.
1074 147, 7, 2016.
1075 Hoerling, M., Eischeid, J., Kumar, A., Leung, R., Mariotti, A., Mo, K., Schubert, S., and
1076 Seager, R.: Causes and Predictability of the 2012 Great Plains Drought, B Am
1077 Meteorol Soc, 95, 269-282, 10.1175/Bams-D-13-00055.1, 2014.
1078 Holben, B. N., Eck, T. F., Slutsker, I., Tanre, D., Buis, J. P., Setzer, A., Vermote, E.,
1079 Reagan, J. A., Kaufman, Y. J., Nakajima, T., Lavenu, F., Jankowiak, I., and
1080 Smirnov, A.: AERONET - A federated instrument network and data archive for
1081 aerosol characterization, Remote Sens Environ, 66, 1-16, Doi 10.1016/S0034-
1082 4257(98)00031-5, 1998.
1083 Holben, B. N., Eck, T. F., Slutsker, I., Smirnov, A., Sinyuk, A., Schafer, J., Giles, D., and
1084 Dubovik, O.: AERONET's Version 2.0 quality assurance criteria, 2006.
1085 Hsu, N. C., Tsay, S. C., King, M. D., and Herman, J. R.: Aerosol properties over bright-
1086 reflecting source regions, Ieee T Geosci Remote, 42, 557-569,
1087 10.1109/Tgrs.2004.824067, 2004.
1088 Hsu, N. C., Jeong, M. J., Bettenhausen, C., Sayer, A. M., Hansell, R., Seftor, C. S.,
1089 Huang, J., and Tsay, S. C.: Enhanced Deep Blue aerosol retrieval algorithm: The

second generation, J Geophys Res-Atmos, 118, 9296-9315, 10.1002/jgrd.50712, 2013.

Huneeus, N., Schulz, M., Balkanski, Y., Griesfeller, J., Prospero, J., Kinne, S., Bauer, S., Boucher, O., Chin, M., Dentener, F., Diehl, T., Easter, R., Fillmore, D., Ghan, S., Ginoux, P., Grini, A., Horowitz, L., Koch, D., Krol, M. C., Landing, W., Liu, X., Mahowald, N., Miller, R., Morcrette, J. J., Myhre, G., Penner, J., Perlwitz, J., Stier, P., Takemura, T., and Zender, C. S.: Global dust model intercomparison in AeroCom phase I, Atmos Chem Phys, 11, 7781-7816, 10.5194/acp-11-7781-2011, 2011.

Jickells, T. D., An, Z. S., Andersen, K. K., Baker, A. R., Bergametti, G., Brooks, N., Cao, J. J., Boyd, P. W., Duce, R. A., Hunter, K. A., Kawahata, H., Kubilay, N., laRoche, J., Liss, P. S., Mahowald, N., Prospero, J. M., Ridgwell, A. J., Tegen, I., and Torres, R.: Global iron connections between desert dust, ocean biogeochemistry, and climate, Science, 308, 67-71, DOI 10.1126/science.1105959, 2005.

Jin, Q., Wei, J., Yang, Z. L., Pu, B., and Huang, J.: Consistent response of Indian summer monsoon to Middle East dust in observations and simulations, Atmos Chem Phys, 15, 9897-9915, 10.5194/acp-15-9897-2015, 2015.

Jin, Q. J., Wei, J. F., and Yang, Z. L.: Positive response of Indian summer rainfall to Middle East dust, Geophys Res Lett, 41, 4068-4074, 10.1002/2014gl059980, 2014.

1111 Jin, Q. J., Yang, Z. L., and Wei, J. F.: Seasonal Responses of Indian Summer Monsoon to
1112 Dust Aerosols in the Middle East, India, and China, J Climate, 29, 6329-6349,
1113 10.1175/Jcli-D-15-0622.1, 2016.
1114 Jones, C. D., Hughes, J. K., Bellouin, N., Hardiman, S. C., Jones, G. S., Knight, J.,
1115 Liddicoat, S., O'Connor, F. M., Andres, R. J., Bell, C., Boo, K. O., Bozzo, A.,
1116 Butchart, N., Cadule, P., Corbin, K. D., Doutriaux-Boucher, M., Friedlingstein,
1117 P., Gornall, J., Gray, L., Halloran, P. R., Hurtt, G., Ingram, W. J., Lamarque, J. F.,
1118 Law, R. M., Meinshausen, M., Osprey, S., Palin, E. J., Chini, L. P., Raddatz, T.,
1119 Sanderson, M. G., Sellar, A. A., Schurer, A., Valdes, P., Wood, N., Woodward,
1120 S., Yoshioka, M., and Zerroukat, M.: The HadGEM2-ES implementation of
1121 CMIP5 centennial simulations, Geosci Model Dev, 4, 543-570, 10.5194/gmd-4-
1122 543-2011, 2011.
1123 Kalnay, E., Kanamitsu, M., Kistler, R., Collins, W., Deaven, D., Gandin, L., Iredell, M.,
1124 Saha, S., White, G., Woollen, J., Zhu, Y., Chelliah, M., Ebisuzaki, W., Higgins,
1125 W., Janowiak, J., Mo, K. C., Ropelewski, C., Wang, J., Leetmaa, A., Reynolds,
1126 R., Jenne, R., and Joseph, D.: The NCEP/NCAR 40-year reanalysis project, B Am
1127 Meteorol Soc, 77, 437-471, Doi 10.1175/1520-
1128 0477(1996)077<0437:Tnyrp>2.0.Co;2, 1996.
1129 Kim, D., Chin, M. A., Bian, H. S., Tan, Q., Brown, M. E., Zheng, T., You, R. J., Diehl,
1130 T., Ginoux, P., and Kucsera, T.: The effect of the dynamic surface bareness on
1131 dust source function, emission, and distribution, J Geophys Res-Atmos, 118, 871-
1132 886, 10.1029/2012jd017907, 2013.

1133 Kim, M. K., Lau, W. K. M., Kim, K. M., Sang, J., Kim, Y. H., and Lee, W. S.:
1134 Amplification of ENSO effects on Indian summer monsoon by absorbing
1135 aerosols, Clim Dynam, 46, 2657-2671, 10.1007/s00382-015-2722-y, 2016.
1136 Knippertz, P.: Dust emissions in the West African heat trough - the role of the diurnal
1137 cycle and of extratropical disturbances, Meteorol Z, 17, 553-563, 10.1127/0941-
1138 2948/2008/0315, 2008.
1139 Kok, J. F., Albani, S., Mahowald, N. M., and Ward, D. S.: An improved dust emission
1140 model - Part 2: Evaluation in the Community Earth System Model, with
1141 implications for the use of dust source functions, Atmos Chem Phys, 14, 13043-
1142 13061, 10.5194/acp-14-13043-2014, 2014a.
1143 Kok, J. F., Mahowald, N. M., Fratini, G., Gillies, J. A., Ishizuka, M., Leys, J. F., Mikami,
1144 M., Park, M. S., Park, S. U., Van Pelt, R. S., and Zobeck, T. M.: An improved
1145 dust emission model - Part 1: Model description and comparison against
1146 measurements, Atmos Chem Phys, 14, 13023-13041, 10.5194/acp-14-13023-
1147 2014, 2014b.
1148 Kurosaki, Y., and Mikami, M.: Effect of snow cover on threshold wind velocity of dust
1149 outbreak, Geophys Res Lett, 31, 10.1029/2003gl018632, 2004.
1150 Kurosaki, Y., and Mikami, M.: Threshold wind speed for dust emission in east Asia and
1151 its seasonal variations, J Geophys Res-Atmos, 112, 10.1029/2006jd007988, 2007.
1152 Largeron, Y., Guichard, F., Bouniol, D., Couvreux, F., Kergoat, L., and Marticorena, B.:
1153 Can we use surface wind fields from meteorological reanalyses for Sahelian dust
1154 emission simulations?, Geophys Res Lett, 42, 2490-2499, 10.1002/2014gl062938,
1155 2015.

1156 Levin, Z., Ganor, E., and Gladstein, V.: The effects of desert particles coated with sulfate
1157 on rain formation in the eastern Mediterranean, J Appl Meteorol, 35, 1511-1523,
1158 Doi 10.1175/1520-0450(1996)035<1511:Teodpc>2.0.Co;2, 1996.
1159 Lin, C. Y., Zhao, C., Liu, X. H., Lin, N. H., and Chen, W. N.: Modelling of long-range
1160 transport of Southeast Asia biomass-burning aerosols to Taiwan and their
1161 radiative forcings over East Asia, Tellus B, 66, 10.3402/tellusb.v66.23733, 2014.
1162 Mahowald, N. M., Baker, A. R., Bergametti, G., Brooks, N., Duce, R. A., Jickells, T. D.,
1163 Kubilay, N., Prospero, J. M., and Tegen, I.: Atmospheric global dust cycle and
1164 iron inputs to the ocean, Global Biogeochem Cy, 19, 10.1029/2004gb002402,
1165 2005.
1166 Mahowald, N. M., Kloster, S., Engelstaedter, S., Moore, J. K., Mukhopadhyay, S.,
1167 McConnell, J. R., Albani, S., Doney, S. C., Bhattacharya, A., Curran, M. A. J.,
1168 Flanner, M. G., Hoffman, F. M., Lawrence, D. M., Lindsay, K., Mayewski, P. A.,
1169 Neff, J., Rothenberg, D., Thomas, E., Thornton, P. E., and Zender, C. S.:
1170 Observed 20th century desert dust variability: impact on climate and
1171 biogeochemistry, Atmos Chem Phys, 10, 10875-10893, 10.5194/acp-10-10875-
1172 2010, 2010.
1173 Malm, W. C., Sisler, J. F., Huffman, D., Eldred, R. A., and Cahill, T. A.: Spatial and
1174 Seasonal Trends in Particle Concentration and Optical Extinction in the United-
1175 States, J Geophys Res-Atmos, 99, 1347-1370, Doi 10.1029/93jd02916, 1994.
1176 Marsham, J. H., Hobby, M., Allen, C. J. T., Banks, J. R., Bart, M., Brooks, B. J.,
1177 Cavazos-Guerra, C., Engelstaedter, S., Gascoyne, M., Lima, A. R., Martins, J. V.,
1178 McQuaid, J. B., O'Leary, A., Ouchene, B., Ouladichir, A., Parker, D. J., Saci, A.,

1179 Salah-Ferroudj, M., Todd, M. C., and Washington, R.: Meteorology and dust in
1180 the central Sahara: Observations from Fennec supersite-1 during the June 2011
1181 Intensive Observation Period, J Geophys Res-Atmos, 118, 4069-4089,
1182 10.1002/jgrd.50211, 2013.
1183 Marticorena, B., and Bergametti, G.: Modeling the Atmospheric Dust Cycle .1. Design of
1184 a Soil-Derived Dust Emission Scheme, J Geophys Res-Atmos, 100, 16415-16430,
1185 Doi 10.1029/95jd00690, 1995.
1186 Marticorena, B., Bergametti, G., Aumont, B., Callot, Y., NDoume, C., and Legrand, M.:
1187 Modeling the atmospheric dust cycle .2. Simulation of Saharan dust sources, J
1188 Geophys Res-Atmos, 102, 4387-4404, Doi 10.1029/96jd02964, 1997.
1189 Marticorena, B., Chatenet, B., Rajot, J. L., Traore, S., Coulibaly, M., Diallo, A., Kone, I.,
1190 Maman, A., Diaye, T. N., and Zakou, A.: Temporal variability of mineral dust
1191 concentrations over West Africa: analyses of a pluriannual monitoring from the
1192 AMMA Sahelian Dust Transect, Atmos Chem Phys, 10, 8899-8915, 10.5194/acp-
1193 10-8899-2010, 2010.
1194 Mbourou, G. N., Bertrand, J. J., and Nicholson, S. E.: The diurnal and seasonal cycles of
1195 wind-borne dust over Africa north of the equator, J Appl Meteorol, 36, 868-882,
1196 Doi 10.1175/1520-0450(1997)036<0868:Tdasco>2.0.Co;2, 1997.
1197 Miller, R. L., and Tegen, I.: Climate response to soil dust aerosols, J Climate, 11, 3247-
1198 3267, Doi 10.1175/1520-0442(1998)011<3247:Crtsda>2.0.Co;2, 1998.
1199 Miller, R. L., Tegen, I., and Perlwitz, J.: Surface radiative forcing by soil dust aerosols
1200 and the hydrologic cycle, J Geophys Res-Atmos, 109, 10.1029/2003jd004085,
1201 2004.

1202 Moorthi, S., and Suarez, M. J.: Relaxed Arakawa-Schubert - a Parameterization of Moist
1203 Convection for General-Circulation Models, Mon Weather Rev, 120, 978-1002,
1204 Doi 10.1175/1520-0493(1992)120<0978:Rasapo>2.0.Co;2, 1992.
1205 Naik, V., Horowitz, L. W., Fiore, A. M., Ginoux, P., Mao, J. Q., Aghedo, A. M., and
1206 Levy, H.: Impact of preindustrial to present-day changes in short-lived pollutant
1207 emissions on atmospheric composition and climate forcing, J Geophys Res-
1208 Atmos, 118, 8086-8110, 10.1002/jgrd.50608, 2013.
1209 Nakajima, T., Higurashi, A., Kawamoto, K., and Penner, J. E.: A possible correlation
1210 between satellite-derived cloud and aerosol microphysical parameters, Geophys
1211 Res Lett, 28, 1171-1174, Doi 10.1029/2000gl012186, 2001.
1212 O'Neill, N. T., Eck, T. F., Smirnov, A., Holben, B. N., and Thulasiraman, S.: Spectral
1213 discrimination of coarse and fine mode optical depth, J Geophys Res-Atmos, 108,
1214 10.1029/2002jd002975, 2003.
1215 O'rgill, M., and Sehmel, G.: Frequency and diurnal variation of dust storms in the
1216 contiguous U.S.A., Atmospheric Environment, 10, 813-825, 1976.
1217 Painter, T. H., Deems, J. S., Belnap, J., Hamlet, A. F., Landry, C. C., and Udall, B.:
1218 Response of Colorado River runoff to dust radiative forcing in snow, P Natl Acad
1219 Sci USA, 107, 17125-17130, 10.1073/pnas.0913139107, 2010.
1220 Painter, T. H., Skiles, S. M., Deems, J. S., Brandt, W. T., and Dozier, J.: Variation in
1221 Rising Limb of Colorado River Snowmelt Runoff Hydrograph Controlled by Dust
1222 Radiative Forcing in Snow, Geophys Res Lett, 45, 797-808,
1223 10.1002/2017gl075826, 2018.

1224 Pu, B., and Ginoux, P.: The impact of the Pacific Decadal Oscillation on springtime dust
1225 activity in Syria, Atmos Chem Phys, 16, 13431-13448, 10.5194/acp-16-13431-
1226 2016, 2016.
1227 Pu, B., and Ginoux, P.: Projection of American dustiness in the late 21st century due to
1228 climate change, Scientific reports, 7, 10.1038/s41598-017-05431-9, 2017.
1229 Pu, B., and Ginoux, P.: Climatic factors contributing to long-term variations in surface
1230 fine dust concentration in the United States, Atmos Chem Phys, 18, 4201-4215,
1231 10.5194/acp-18-4201-2018, 2018a.
1232 Pu, B., and Ginoux, P.: How reliable are CMIP5 models in simulating dust optical
1233 depth?, Atmos Chem Phys, 18, 12491-12510, 10.5194/acp-18-12491-2018,
1234 2018b.
1235 Putman, W. M., and Lin, S. H.: Finite-volume transport on various cubed-sphere grids, J
1236 Comput Phys, 227, 55-78, 10.1016/j.jcp.2007.07.022, 2007.
1237 Raupach, M. R., Gillette, D. A., and Leys, J. F.: The Effect of Roughness Elements on
1238 Wind Erosion Threshold, J Geophys Res-Atmos, 98, 3023-3029, Doi
1239 10.1029/92jd01922, 1993.
1240 Rayner, N. A., Parker, D. E., Horton, E. B., Folland, C. K., Alexander, L. V., Rowell, D.
1241 P., Kent, E. C., and Kaplan, A.: Global analyses of sea surface temperature, sea
1242 ice, and night marine air temperature since the late nineteenth century, J Geophys
1243 Res-Atmos, 108, 10.1029/2002jd002670, 2003.
1244 Reid, J. S., Hyer, E. J., Prins, E. M., Westphal, D. L., Zhang, J. L., Wang, J., Christopher,
1245 S. A., Curtis, C. A., Schmidt, C. C., Eleuterio, D. P., Richardson, K. A., and
1246 Hoffman, J. P.: Global Monitoring and Forecasting of Biomass-Burning Smoke:

Description of and Lessons From the Fire Locating and Modeling of Burning Emissions (FLAMBE) Program, Ieee J-Stars, 2, 144-162, 10.1109/Jstars.2009.2027443, 2009.

Reynolds, R. W., Rayner, N. A., Smith, T. M., Stokes, D. C., and Wang, W. Q.: An improved in situ and satellite SST analysis for climate, J Climate, 15, 1609-1625, Doi 10.1175/1520-0442(2002)015<1609:Aiisas>2.0.Co;2, 2002.

Rieger, D., Steiner, A., Bachmann, V., Gasch, P., Forstner, J., Deetz, K., Vogel, B., and Vogel, H.: Impact of the 4 April 2014 Saharan dust outbreak on the photovoltaic power generation in Germany, Atmos Chem Phys, 17, 13391-13415, 10.5194/acp-17-13391-2017, 2017.

Rienecker, M. M., Suarez, M. J., Todling, R., Bacmeister, J., Takacs, L., Liu, H.-C., Gu, W., Sienkiewicz, M., Koster, R. D., Gelaro, R., Stajner, I., and Nielsen, J. E.: The GEOS‐5 Data Assimilation System−Documentation of versions 5.0.1, 5.1.0, and 5.2.0, Technical Report Series on Global Modeling and Data Assimilation, 27 (available at http://gmao.gsfc.nasa.gov/pubs/docs/Rienecker369.pdf), 2008.

Rosenfield, J. E., Considine, D. B., Meade, P. E., Bacmeister, J. T., Jackman, C. H., and Schoeberl, M. R.: Stratospheric effects of Mount Pinatubo aerosol studied with a coupled two-dimensional model, J Geophys Res-Atmos, 102, 3649-3670, Doi 10.1029/96jd03820, 1997.

Savoie, D. L., and Prospero, J. M.: Comparison of Oceanic and Continental Sources of Non-Sea-Salt Sulfate over the Pacific-Ocean, Nature, 339, 685-687, DOI 10.1038/339685a0, 1989.

1269 Sayer, A. M., Hsu, N. C., Bettenhausen, C., and Jeong, M. J.: Validation and uncertainty
1270 estimates for MODIS Collection 6 "Deep Blue" aerosol data, J Geophys Res-
1271 Atmos, 118, 7864-7872, 10.1002/jgrd.50600, 2013.
1272 Schepanski, K., Tegen, I., Laurent, B., Heinold, B., and Macke, A.: A new Saharan dust
1273 source activation frequency map derived from MSG-SEVIRI IR-channels,
1274 Geophys Res Lett, 34, 10.1029/2007gl030168, 2007.
1275 Schepanski, K., Tegen, I., Todd, M. C., Heinold, B., Bonisch, G., Laurent, B., and
1276 Macke, A.: Meteorological processes forcing Saharan dust emission inferred from
1277 MSG-SEVIRI observations of subdaily dust source activation and numerical
1278 models, J Geophys Res-Atmos, 114, 10.1029/2008jd010325, 2009.
1279 Shao, Y.: A model for mineral dust emission, J Geophys Res-Atmos, 106, 20239-20254,
1280 Doi 10.1029/2001jd900171, 2001.
1281 Shao, Y. P., Wyrwoll, K. H., Chappell, A., Huang, J. P., Lin, Z. H., McTainsh, G. H.,
1282 Mikami, M., Tanaka, T. Y., Wang, X. L., and Yoon, S.: Dust cycle: An emerging
1283 core theme in Earth system science, Aeolian Res, 2, 181-204,
1284 10.1016/j.aeolia.2011.02.001, 2011.
1285 Sharma, D., and Miller, R. L.: Revisiting the observed correlation between weekly
1286 averaged Indian monsoon precipitation and Arabian Sea aerosol optical depth,
1287 Geophys Res Lett, 44, 10006-10016, 10.1002/2017gl074373, 2017.
1288 Solmon, F., Nair, V. S., and Mallet, M.: Increasing Arabian dust activity and the Indian
1289 summer monsoon, Atmos Chem Phys, 15, 8051-8064, 10.5194/acp-15-8051-
1290 2015, 2015.

1291 Strong, J. D., Vecchi, G. A., and Ginoux, P.: The Climatological Effect of Saharan Dust
1292 on Global Tropical Cyclones in a Fully Coupled GCM, Journal of Geophysical
1293 Research - Atmospheres, 123, https://doi.org/10.1029/2017JD027808, 2018.
1294 Strong, J. D. O., Vecchi, G. A., and Ginoux, P.: The Response of the Tropical Atlantic
1295 and West African Climate to Saharan Dust in a Fully Coupled GCM, J Climate,
1296 28, 7071-7092, 10.1175/Jcli-D-14-00797.1, 2015.
1297 Takemura, T., Okamoto, H., Maruyama, Y., Numaguti, A., Higurashi, A., and Nakajima,
1298 T.: Global three-dimensional simulation of aerosol optical thickness distribution
1299 of various origins, J Geophys Res-Atmos, 105, 17853-17873, Doi
1300 10.1029/2000jd900265, 2000.
1301 Taylor, K., Williamson, D., and Zwiers, F.: The sea surface temperature and sea ice
1302 concentration boundary conditions for AMIP II simulations (PCMDI Rep. 60, pp.
1303 1–25), Livermore, CA:Program for Climate Model Diagnosis and
1304 Intercomparison, Lawrence Livermore National Laboratory, 2000.
1305 Tegen, I., and Fung, I.: Modeling of Mineral Dust in the Atmosphere - Sources,
1306 Transport, and Optical-Thickness, J Geophys Res-Atmos, 99, 22897-22914, Doi
1307 10.1029/94jd01928, 1994.
1308 Tong, D. Q., Wang, J. X. L., Gill, T. E., Lei, H., and Wang, B. Y.: Intensified dust storm
1309 activity and Valley fever infection in the southwestern United States, Geophys
1310 Res Lett, 44, 4304-4312, 10.1002/2017gl073524, 2017.
1311 Uno, I., Amano, H., Emori, S., Kinoshita, K., Matsui, I., and Sugimoto, N.: Trans-Pacific
1312 yellow sand transport observed in April 1998: A numerical simulation, J Geophys
1313 Res-Atmos, 106, 18331-18344, Doi 10.1029/2000jd900748, 2001.

1314 Vinoj, V., Rasch, P. J., Wang, H. L., Yoon, J. H., Ma, P. L., Landu, K., and Singh, B.:
1315 Short-term modulation of Indian summer monsoon rainfall by West Asian dust,
1316 Nat Geosci, 7, 308-313, 10.1038/ngeo2107, 2014.
1317 Watanabe, S., Hajima, T., Sudo, K., Nagashima, T., Takemura, T., Okajima, H., Nozawa,
1318 T., Kawase, H., Abe, M., Yokohata, T., Ise, T., Sato, H., Kato, E., Takata, K.,
1319 Emori, S., and Kawamiya, M.: MIROC-ESM 2010: model description and basic
1320 results of CMIP5-20c3m experiments, Geosci Model Dev, 4, 845-872,
1321 10.5194/gmd-4-845-2011, 2011.
1322 Westphal, D. L., Curtis, C. A., Liu, M., and Walker, A. L.: Operational aerosol and dust
1323 storm forecasting, in WMO/GEO Expert Meeting on an International Sand and
1324 Dust Storm Warning System, IOP Conference Series Earth and Environmental
1325 Science, 2009.
1326 Winker, D. M., Hunt, W., and Hostetler, C.: Status and performance of the CALIOP
1327 lidar, Bba Lib, 5575, 8-15, 10.1117/12.571955, 2004.
1328 Winker, D. M., Hunt, W. H., and McGill, M. J.: Initial performance assessment of
1329 CALIOP, Geophys Res Lett, 34, 10.1029/2007gl030135, 2007.
1330 Witek, M. L., Flatau, P. J., Quinn, P. K., and Westphal, D. L.: Global sea-salt modeling:
1331 Results and validation against multicampaign shipboard measurements, J
1332 Geophys Res-Atmos, 112, 10.1029/2006jd007779, 2007.
1333 Wong, S., and Dessler, A. E.: Suppression of deep convection over the tropical North
1334 Atlantic by the Saharan Air Layer, Geophys Res Lett, 32, 10.1029/2004gl022295,
1335 2005.

Wurzler, S., Reisin, T. G., and Levin, Z.: Modification of mineral dust particles by cloud processing and subsequent effects on drop size distributions, J Geophys Res-Atmos, 105, 4501-4512, Doi 10.1029/1999jd900980, 2000.

Yan, K., Park, T., Yan, G. J., Chen, C., Yang, B., Liu, Z., Nemani, R. R., Knyazikhin, Y., and Myneni, R. B.: Evaluation of MODIS LAI/FPAR Product Collection 6. Part 1: Consistency and Improvements, Remote Sens-Basel, 8, 10.3390/rs8050359, 2016a.

Yan, K., Park, T., Yan, G. J., Liu, Z., Yang, B., Chen, C., Nemani, R. R., Knyazikhin, Y., and Myneni, R. B.: Evaluation of MODIS LAI/FPAR Product Collection 6. Part 2: Validation and Intercomparison, Remote Sens-Basel, 8, 10.3390/rs8060460, 2016b.

Yu, H. B., Chin, M., Yuan, T. L., Bian, H. S., Remer, L. A., Prospero, J. M., Omar, A., Winker, D., Yang, Y. K., Zhang, Y., Zhang, Z. B., and Zhao, C.: The fertilizing role of African dust in the Amazon rainforest: A first multiyear assessment based on data from Cloud-Aerosol Lidar and Infrared Pathfinder Satellite Observations, Geophys Res Lett, 42, 1984-1991, 10.1002/2015gl063040, 2015.

Zender, C. S., Bian, H. S., and Newman, D.: Mineral Dust Entrainment and Deposition (DEAD) model: Description and 1990s dust climatology, J Geophys Res-Atmos, 108, 10.1029/2002jd002775, 2003.

Zhao, M., Golaz, J. C., Held, I. M., Guo, H., Balaji, V., Benson, R., Chen, J. H., Chen, X., Donner, L. J., Dunne, J. P., Dunne, K., Durachta, J., Fan, S. M., Freidenreich, S. M., Garner, S. T., Ginoux, P., Harris, L. M., Horowitz, L. W., Krasting, J. P., Langenhorst, A. R., Liang, Z., Lin, P., Lin, S. J., Malyshev, S. L., Mason, E.,

1359 Milly, P. C. D., Ming, Y., Naik, V., Paulot, F., Paynter, D., Phillipps, P.,
1360 Radhakrishnan, A., Ramaswamy, V., Robinson, T., Schwarzkopf, D., Seman, C.
1361 J., Shevliakova, E., Shen, Z., Shin, H., Silvers, L. G., Wilson, J. R., Winton, M.,
1362 Wittenberg, A. T., Wyman, B., and Xiang, B.: The GFDL Global Atmosphere and
1363 Land Model AM4.0/LM4.0:1. Simulation Characteristics With Prescribed SSTs, J
1364 Adv Model Earth Sy, 10, 691-734, 10.1002/2017ms001208, 2018a.
1365 Zhao, M., Golaz, J. C., Held, I. M., Guo, H., Balaji, V., Benson, R., Chen, J. H., Chen,
1366 X., Donner, L. J., Dunne, J. P., Dunne, K., Durachta, J., Fan, S. M., Freidenreich,
1367 S. M., Garner, S. T., Ginoux, P., Harris, L. M., Horowitz, L. W., Krasting, J. P.,
1368 Langenhorst, A. R., Liang, Z., Lin, P., Lin, S. J., Malyshev, S. L., Mason, E.,
1369 Milly, P. C. D., Ming, Y., Naik, V., Paulot, F., Paynter, D., Phillipps, P.,
1370 Radhakrishnan, A., Ramaswamy, V., Robinson, T., Schwarzkopf, D., Seman, C.
1371 J., Shevliakova, E., Shen, Z., Shin, H., Silvers, L. G., Wilson, J. R., Winton, M.,
1372 Wittenberg, A. T., Wyman, B., and Xiang, B.: The GFDL Global Atmosphere and
1373 Land Model AM4.0/LM4.0:2. Model Description, Sensitivity Studies, and Tuning
1374 Strategies, J Adv Model Earth Sy, 10, 735-769, 10.1002/2017ms001209, 2018b.
1375

Table 1 Major dust source regions shown in Figure 1. Note that region names such as India and northern China are not exactly the same as their geographical definitions but also cover some areas from nearby countries.

Table 2 Sensitivity of annual mean wind erosion threshold (m s^{-1}) to the selection of different retrieval criteria. Note the setting of the last column is the same as DOD_{thresh}=0.2 or 0.02, except surface DOD (sDOD) from Aqua is used over North Africa. Here DOD_{thresh}=0.2 or 0.5 is applied to dusty regions, i.e., the Sahel, Sahara, Arabian Peninsula, northern China, and India, while DOD_{thresh}=0.02 or 0.05 is applied to less dusty regions, i.e., the U.S., South Africa, South America, and Australia.

Table 3 Sensitivity of annual mean wind erosion threshold (m s^{-1}) to surface wind speeds from different reanalyses (DOD_{thresh}= 0.2 or 0.02).

Table 4 Simulation design

1399

1400

1401

1402 Figure 1. (a)-(e) Frequencies of occurrence (FoO; unit: days per season) in each season
1403 and annual mean. (f)-(j) Threshold of wind erosion ($V_{threshold;}$ unit: m s^{-1}) derived from
1404 satellite products and reanalyses for each season and annual mean using DOD_{thresh}=0.2
1405 (or 0.02). Black boxes in (f) denote nine dust source regions as listed in Table 1.

1406

1407 Figure 2. (a)-(i) Frequency distribution of annual mean $V_{threshold}$ (black bars) in each
1408 region (black boxes in Fig. 1) and for dusty seasons, i.e., MAM (green) and JJA (blue)
1409 for regions in the Northern Hemisphere and SON (orange) and DJF (grey) for regions in
1410 the Southern Hemisphere. The mean (averaged over all grid points in the region, without
1411 area weight) and ± one standard deviations of $V_{threshold}$ in each region are shown on the
1412 top right of each plot.

1413

1414 Figure 3. (a)-(e) Threshold of wind erosion ($V_{threshold;}$ unit: m s^{-1}) derived from satellite
1415 products and reanalyses for each season and annual mean using DOD_{thresh}=0.5 (or 0.05).
1416 Black boxes in (a) denote nine dust source regions as listed in Table 1.

1417

1418 Figure 4. Climatology of annual mean AERONET (a) AOD (550 nm) and (b) SDA COD
1419 (500 nm) averaged over 2003-2015.

1420

1421 Figure 5. Scatter plot of simulated annual mean (a) AOD and (b) COD in the Control run
1422 versus AERONET AOD and COD (left), and the relative difference (in percentage) (c)
1423 between modeled AOD and AERONET AOD and (d) between modeled COD and
1424 AERONET COD (right). (e) The relative contribution of DOD to COD in the model.
1425 Figure 6. Same as Fig. 5 but for the V_{thresh}12mn simulation.
1426
1427 Figure 7. (a) Climatology (2003-2015) of AERONET DOD (550 nm) over major dusty
1428 regions and (b) scatter plot of modeled DOD in the V_{thresh}12mn simulation versus
1429 AERONET DOD, and (c) the relative difference (in percentage) between modeled DOD
1430 and AERONET DOD in the V_{thresh}12mn simulation.
1431
1432 Figure 8. Regional averaged annual mean DOD (2003-2015) over nine regions from the
1433 Control (grey), V_{thresh}12mn (orange), and V_{thresh}Ann (yellow) simulations and MODIS
1434 (black).
1435
1436 Figure 9. Scatter plots (left column) of model simulated (from top to bottom are the
1437 Control, V_{thresh}Ann, and V_{thresh}12mn simulations) surface dust concentration versus the
1438 climatology of observed surface dust concentration from RSMAS stations (Savoie and
1439 Prospero 1989), and spatial pattern of surface dust concentration from model output
1440 (shading; right column) and the ratio between modeled and RSMAS station observed
1441 surface dust concentration (color triangles, with upward triangles indicating
1442 overestimation and downward triangles indicating underestimation). 16 stations were
1443 used, and numbers in each triangle (right) and grey dots (left) indicate the stations. The

1444 one-one, one-two and one-five lines are plotted in solid, dashed and dash-dotted lines in
1445 the scatter plots. Statistics in the scatter plots are calculated in logarithmic space.
1446
1447 Figure 10. Annual mean surface fine dust concentration (μg m^{-3}) from IMPROVE
1448 stations (left column) and three simulations (middle column) and the differences between
1449 model and observation (right column) for 2002-2015.
1450
1451 Figure 11. Seasonal cycle of DOD from MODIS (black), the Control (grey), V_{thresh}12mn
1452 (orange), and V_{thresh}Ann (yellow) runs, and gridded AERONET SDA COD (blue)
1453 averaged over nine regions. The annual mean of each dataset in each region is listed on
1454 the top of the plot.
1455
1456 Figure 12. Seasonal cycle of DOD over 12 AERONET SDA sites (see Fig. S7 in the
1457 Supplement for locations) from the Control (grey), V_{thresh}12mn (orange), and V_{thresh}Ann
1458 (yellow) simulations, along with DOD from MODIS (blue), and COD from AERONET
1459 (black dotted line). All values are averaged over 2003-2015. The location (lat/long) and
1460 the name (due to space, only first seven characters are shown) of the sites are listed at the
1461 top of each plot.
1462
1463 Figure 13. (a)-(c) Seasonal cycle of PM_{10} surface concentration (black) over three sites
1464 from the LISA project, along with PM_{10} surface dust concentration from the Control
1465 (grey), V_{thresh}12mn (orange), and V_{thresh}Ann (yellow) simulations. Error bars are ± one
1466 standard deviations of daily mean in each month averaged over 2006-2014. Unites: μg m^{-}

1467 ^{3}. (d)-(f) seasonal cycle of DOD (550 nm) from three AERONET sites co-located with
1468 LISA sites (blue) versus that modeled by the Control (grey), V_{thresh}12mn (orange), and
1469 V_{thresh}Ann (yellow) simulations.
1470 Figure 14. Daily DOD from MODIS (top panel), daily DOD simulated by the V_{thresh}12mn
1471 run along with anomalies (with reference to the 2000-2015 mean) of surface wind vectors
1472 (m s^{-1}; bottom panel) from Oct. 17th to Oct. 19th, 2012. Only DOD over land is shown.
1473 Missing values in MODIS DOD (top panel) are plotted in grey shading.
1474
1475 Figure 15. Frequency (%) distribution of regional averaged daily DOD from MODIS
1476 (black) versus that from the Control (light blue) and V_{thresh}12mn (orange) simulations for
1477 the Sahara, the Sahel, the Arabian Peninsula, northern China, India, western to central
1478 U.S., South America, South Africa, and Australia from 2003 to 2015. X-axis denotes the
1479 ranges of DOD (the bin spacing for dusty regions is 0.05 and for less dusty regions is
1480 0.01), and y-axis is percentage of occurrence. The light green boxes denote the averaging
1481 areas. For regions in the Northern Hemisphere frequency in MAM is shown, while for
1482 regions in the Southern Hemisphere frequency in SON is shown.
1483
1484
1485
1486
1487
1488
1489
1490
1491
1492

Table 1 Major dust source regions shown in Figure 1. Note that region names such as India and northern China are not exactly the same as their geographical definitions but also cover some areas from nearby countries.

No.	Regions	Lat/long
1	Sahel	10°-20°N, 18°W-35°E
2	Sahara	20°-35°N, 15°W-25°E
3	Arabian Peninsula	15°-35°N, 35°-60°E
4	Northern China (N. China)	35°-45°N, 77°-103°E
5	India	20°-35°N, 60°-85°E
6	U.S.	25°-45°N, 102°-125°W
7	South Africa (S. Africa)	17°-35°S, 15°-30°E
8	South America (S. America)	18°-55°S, 65°-75°W
9	Australia	15°-35°S, 128-147°E

Table 2 Sensitivity of annual mean wind erosion threshold (m s^{-1}) to the selection of different retrieval criteria. Note the setting of the last column is the same as DOD_{thresh}=0.2 or 0.02, except surface DOD (sDOD) from Aqua is used over North Africa. Here DOD_{thresh}=0.2 or 0.5 is applied to dusty regions, i.e., the Sahel, Sahara, Arabian Peninsula, northern China, and India, while DOD_{thresh}=0.02 or 0.05 is applied to less dusty regions, i.e., the U.S., South Africa, South America, and Australia.

Regions	**Soil Moisture (cm^3 cm^{-3})**			**LAI (m^2m^{-2})**			**Snow coverage (%)**			**DOD_{thresh}**		
	<0.1	<0.15	None	<0.15	<0.3	<0.5	<=0.2	<=2	<=10	=0.2 (0.02)	=0.5 (0.05)	sDOD
Sahel	3.21	3.19	3.22	3.24	3.21	3.19	3.21	3.21	3.21	3.21	4.93	6.05
Sahara	4.61	4.56	4.49	4.54	4.61	4.59	4.61	4.61	4.61	4.61	7.59	7.66
AP	5.37	5.26	5.26	5.26	5.37	5.37	5.37	5.36	5.35	5.37	8.00	5.57
N. China	7.73	7.64	7.07	7.79	7.73	7.71	7.73	7.56	7.44	7.73	10.15	7.73
India	5.63	5.12	4.99	6.46	5.63	5.63	5.63	5.61	5.60	5.63	8.59	5.63
U.S.	5.71	5.23	4.98	6.53	5.71	5.56	5.71	5.60	5.41	5.71	7.04	5.71
S. Africa	5.41	5.23	5.20	6.72	5.41	5.10	5.41	5.40	5.40	5.41	6.46	5.41
S. America	6.46	6.32	6.20	6.88	6.46	6.39	6.46	6.39	6.35	6.46	8.20	6.46
Australia	5.19	5.16	5.14	5.66	5.19	5.22	5.19	5.19	5.19	5.19	6.49	5.19

Table 3 Sensitivity of annual mean wind erosion threshold (m s^{-1}) to surface wind speeds from different reanalyses (DOD_{thresh}= 0.2 or 0.02).

Regions	**Reanalysis**		
	NCEP	ERA-Interim	ERA5
Sahel	3.21	4.54	4.80
Sahara	4.61	5.56	5.63
AP	5.37	6.12	5.50
N. China	7.73	7.94	7.05
India	5.63	7.01	5.70
U.S.	5.71	6.82	6.18
S. Africa	5.41	7.17	6.26
S. America	6.46	7.51	6.36
Australia	5.19	7.36	6.68

Table 4 Simulation design

Simulations	**Wind erosion threshold**	**Source function**
Control	6 m s^{-1}	*S*
V_{thresh}12mn	12-month $V_{threshold}$	*S'*
V_{thresh}Ann	Annual mean $V_{threshold}$	*S'*

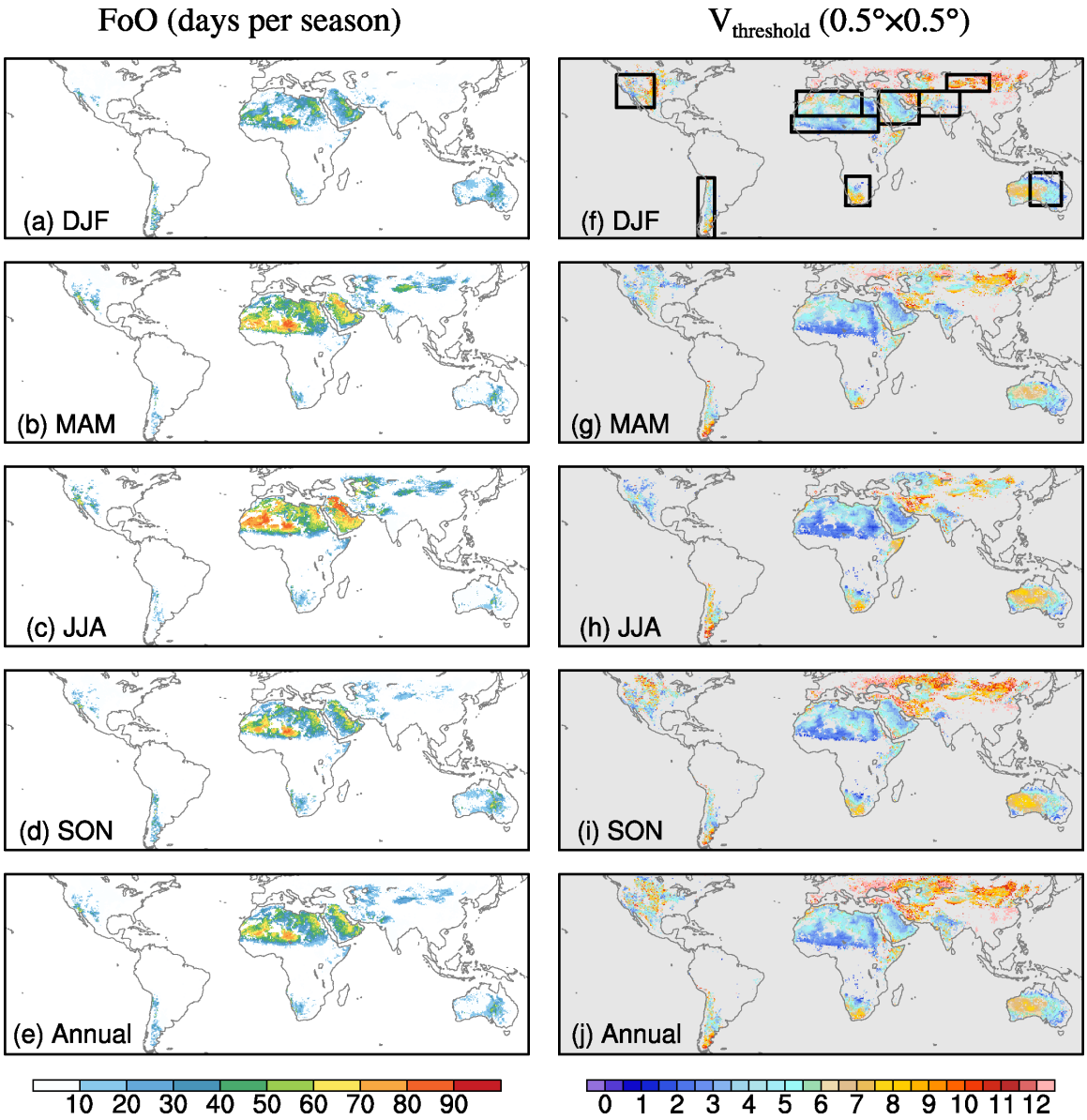

Figure 1. (a)-(e) Frequencies of occurrence (FoO; unit: days per season) in each season and annual mean. (f)-(j) Threshold of wind erosion ($V_{threshold}$; unit: m s^{-1}) derived from satellite products and reanalyses for each season and annual mean using DOD_{thresh} = 0.2 (or 0.02). Black boxes in (f) denote nine dust source regions as listed in Table 1.

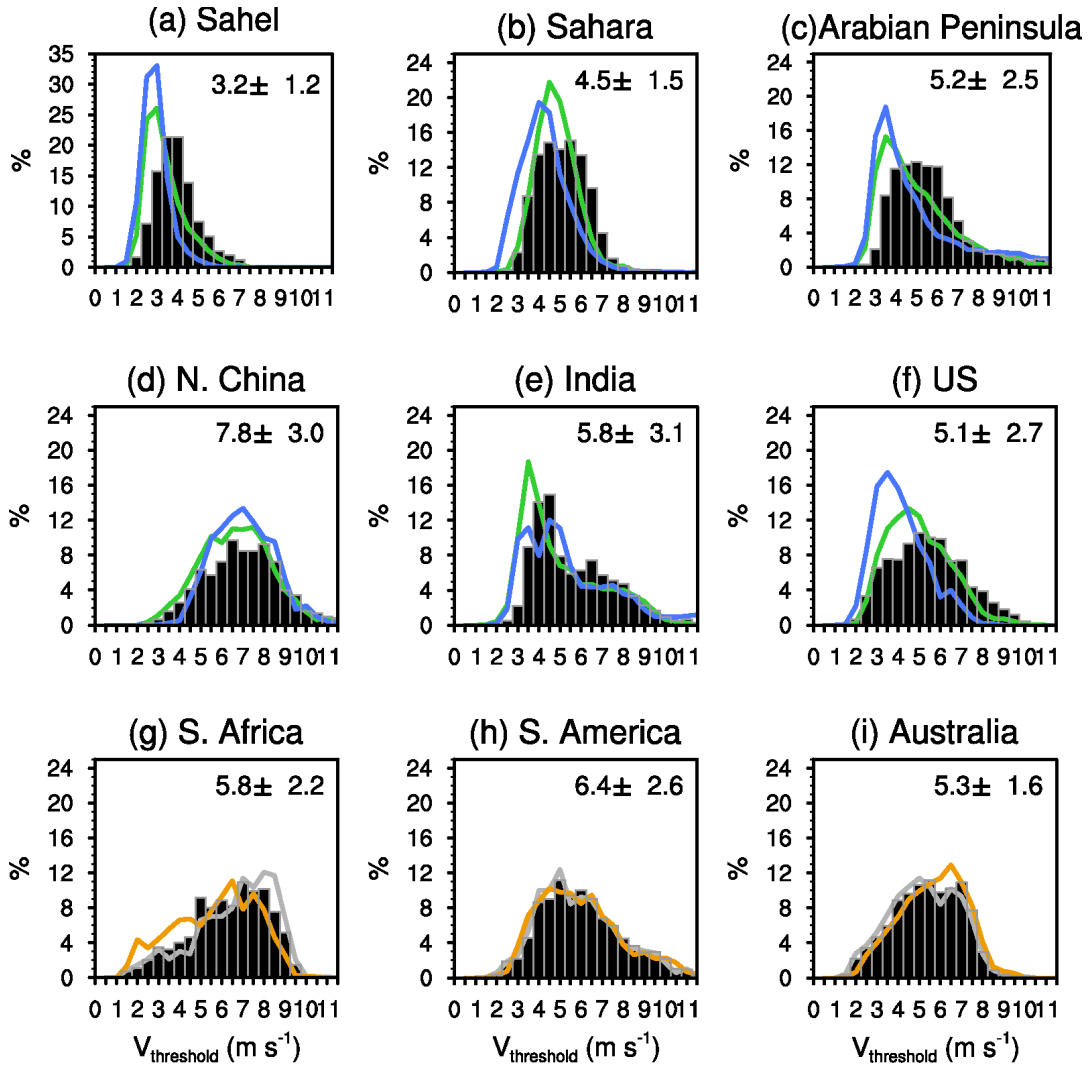

Figure 2. (a)-(i) Frequency distribution of annual mean $V_{threshold}$ (black bars) in each region (black boxes in Fig. 1) and for dusty seasons, i.e., MAM (green) and JJA (blue) for regions in the Northern Hemisphere and SON (orange) and DJF (grey) for regions in the Southern Hemisphere. The mean (averaged over all grid points in the region, without area weight) and ± one standard deviations of $V_{threshold}$ in each region are shown on the top right of each plot.

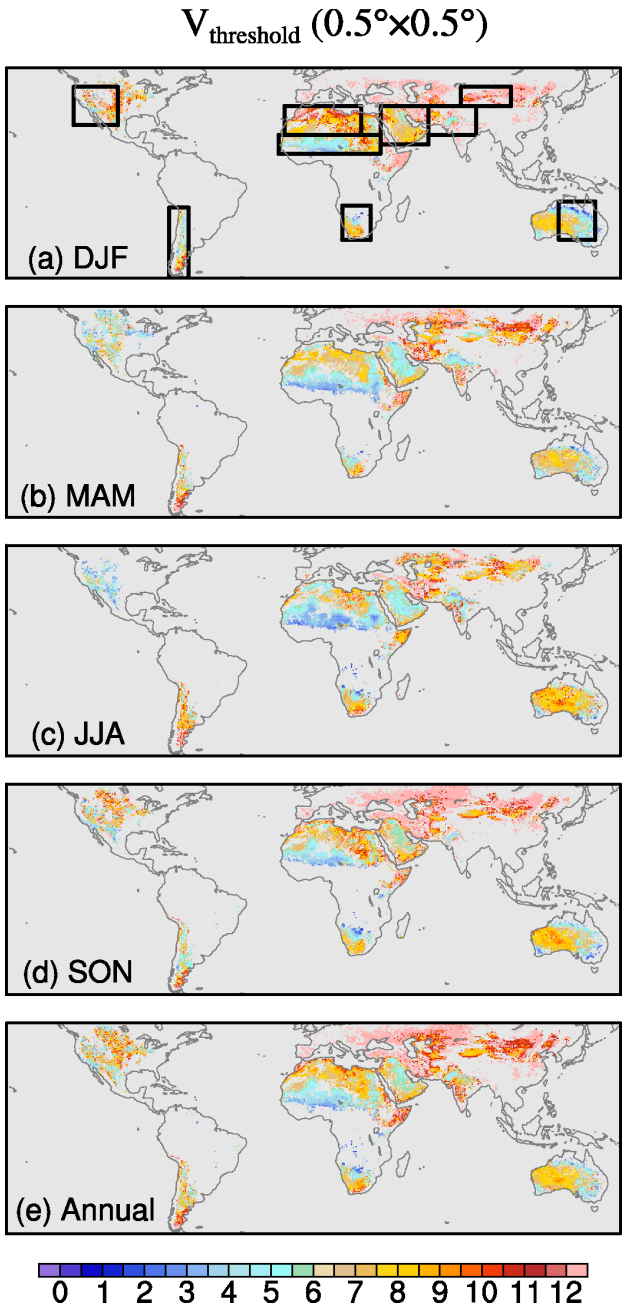

Figure 3. (a)-(e) Threshold of wind erosion ($V_{threshold}$; unit: m s^{-1}) derived from satellite products and reanalyses for each season and annual mean using DOD_{thresh}=0.5 (or 0.05). Black boxes in (a) denote nine dust source regions as listed in Table 1.

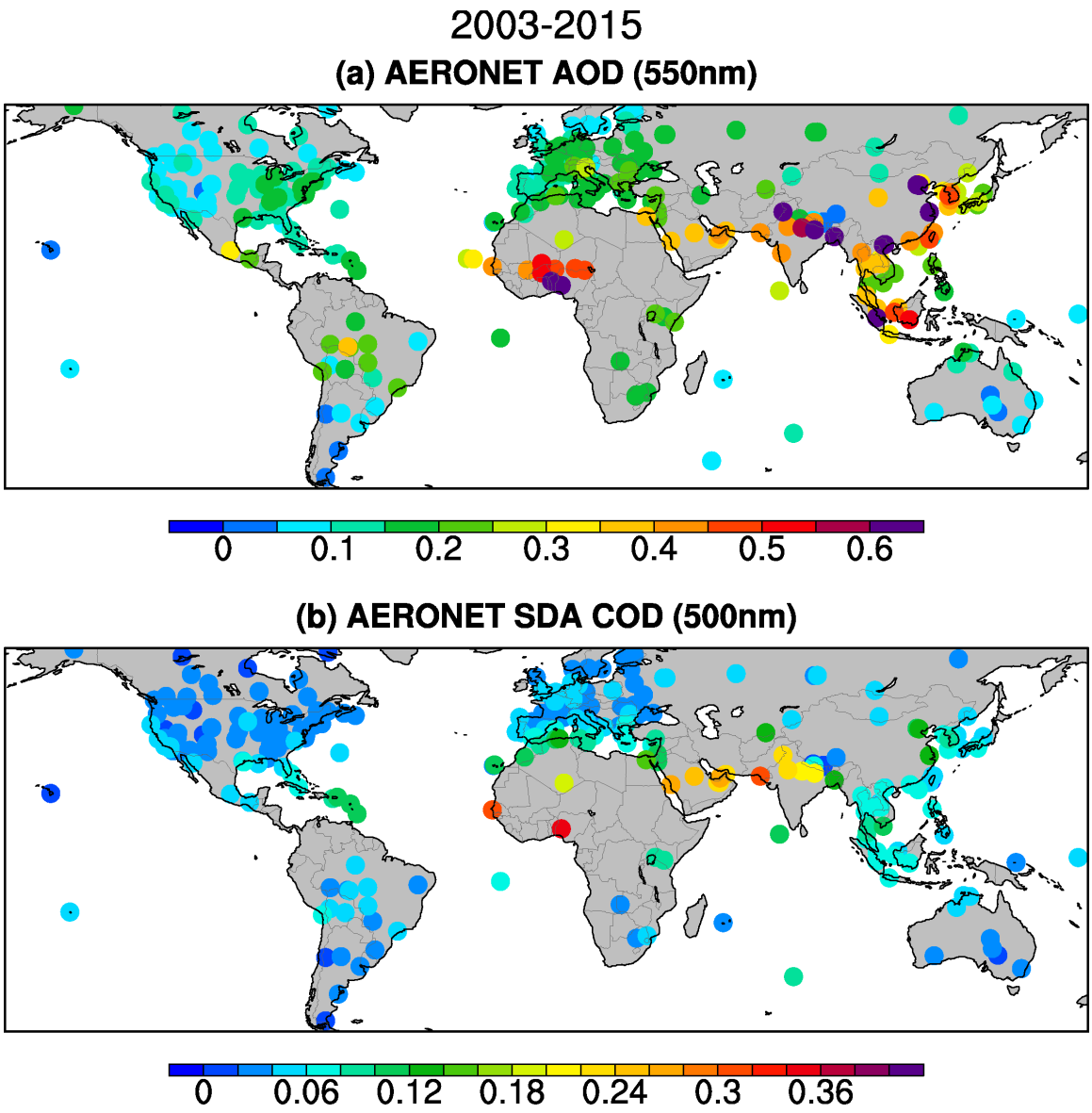

Figure 4. Climatology of annual mean AERONET (a) AOD (550 nm) and (b) SDA COD (500 nm) averaged over 2003-2015.

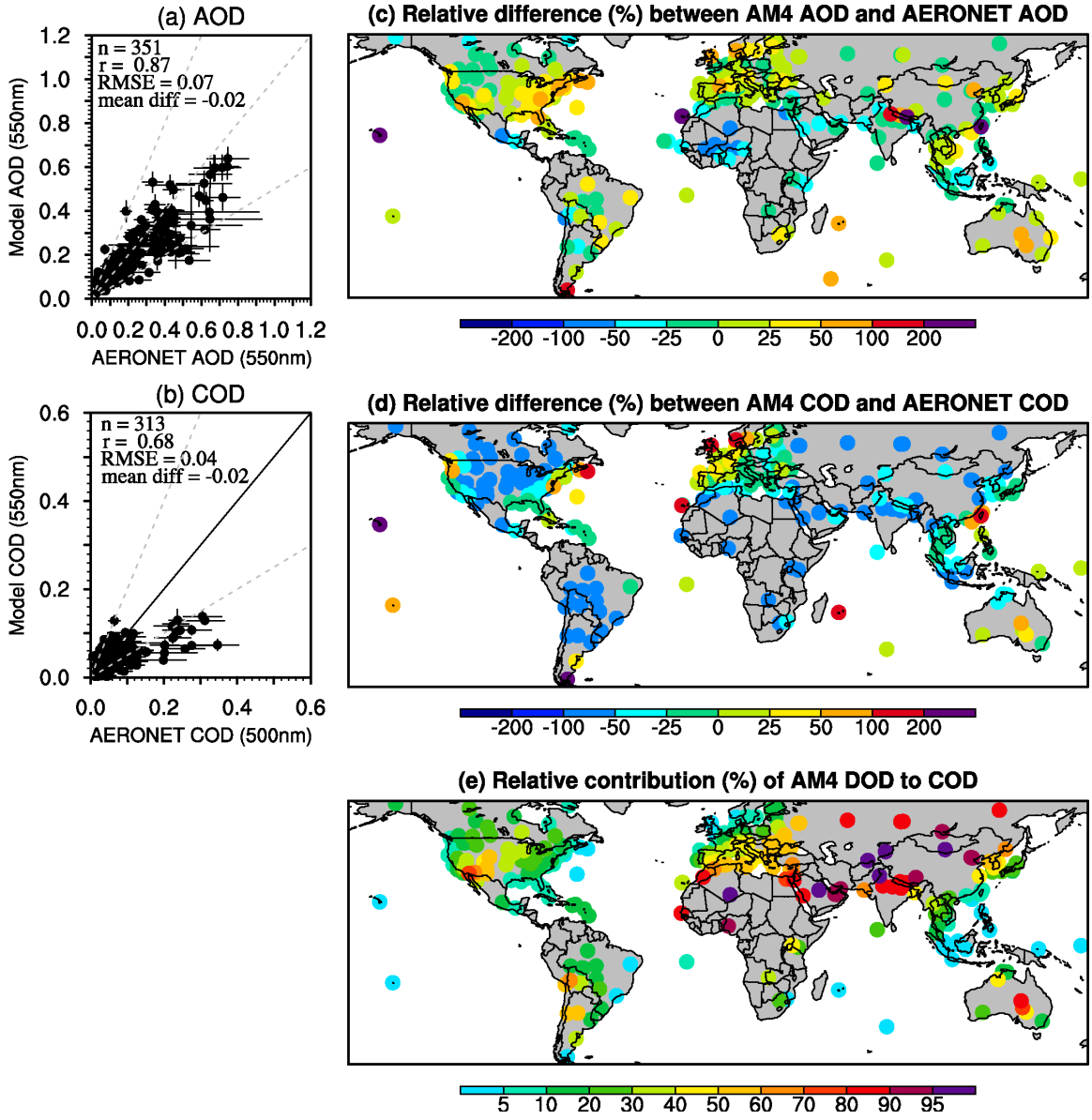

Figure 5. Scatter plot of simulated annual mean (a) AOD and (b) COD in the Control run versus AERONET AOD and COD (left), and the relative difference (in percentage) (c) between modeled AOD and AERONET AOD and (d) between modeled COD and AERONET COD (right). (e) The relative contribution of DOD to COD in the model.

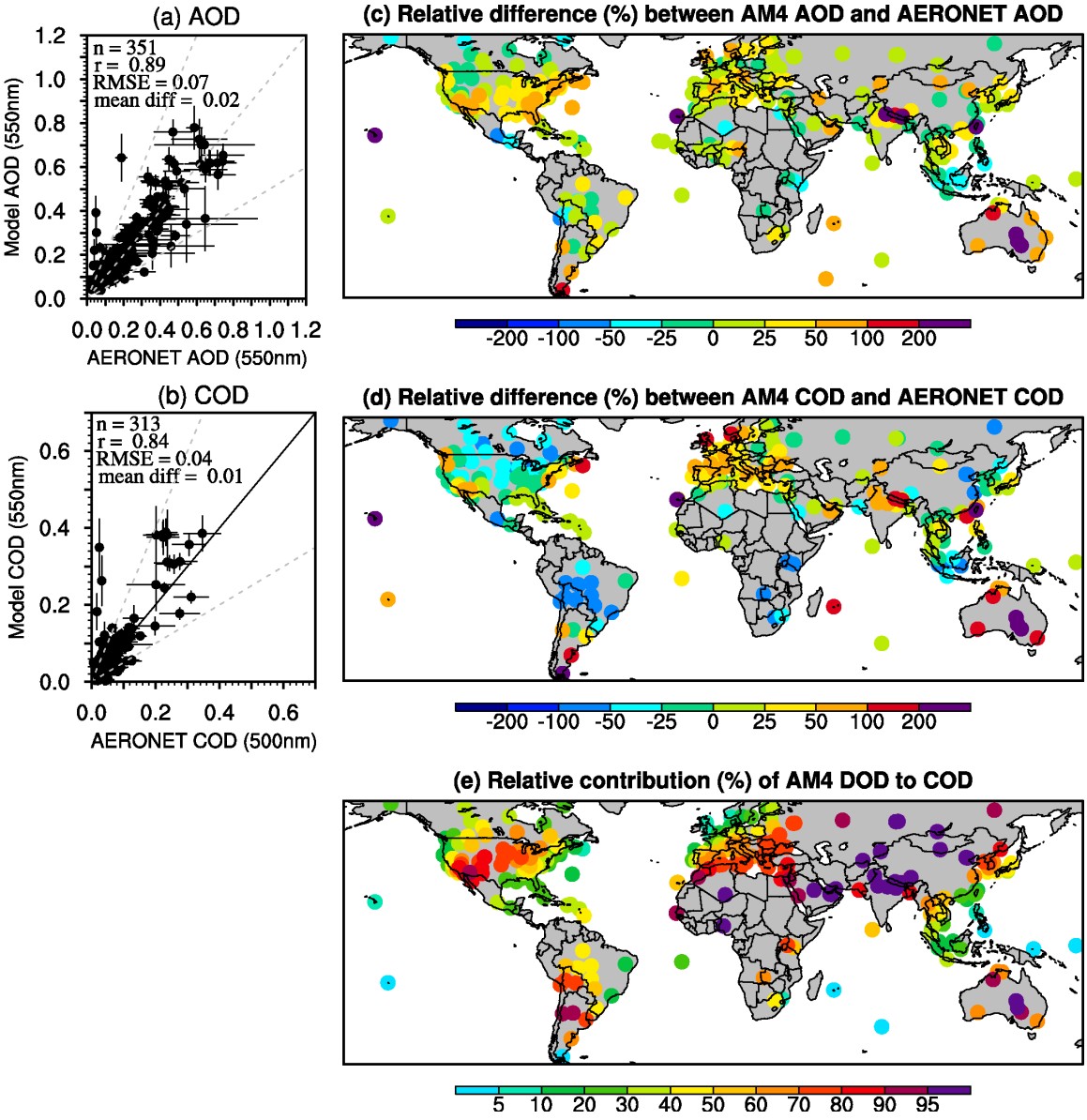

Figure 6. Same as Fig. 5 but for the V_{thresh}12mn simulation.

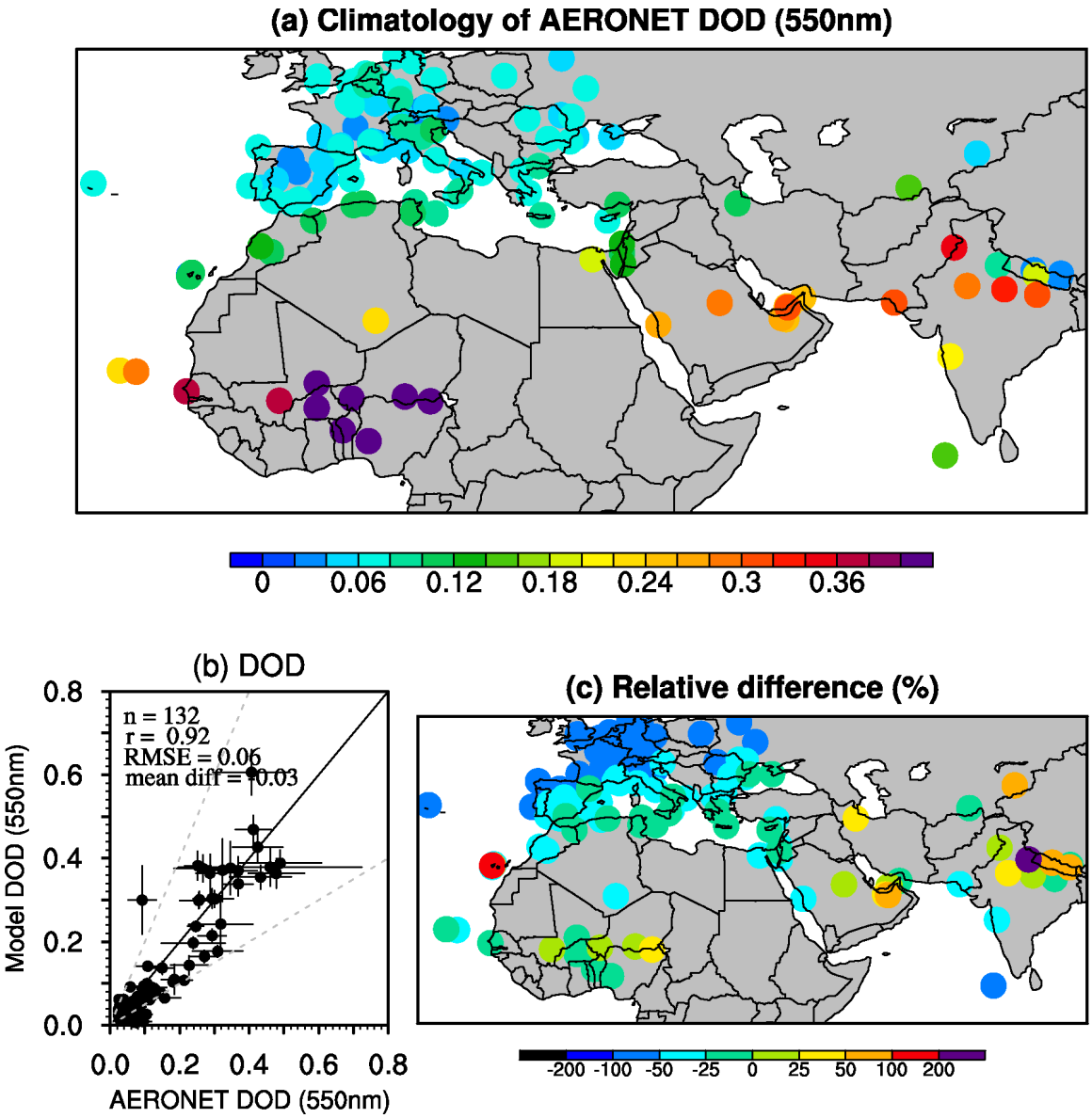

Figure 7. (a) Climatology (2003-2015) of AERONET DOD (550 nm) over major dusty regions and (b) scatter plot of modeled DOD in the V_{thresh}12mn simulation versus AERONET DOD, and (c) the relative difference (in percentage) between modeled DOD and AERONET DOD in the V_{thresh}12mn simulation.

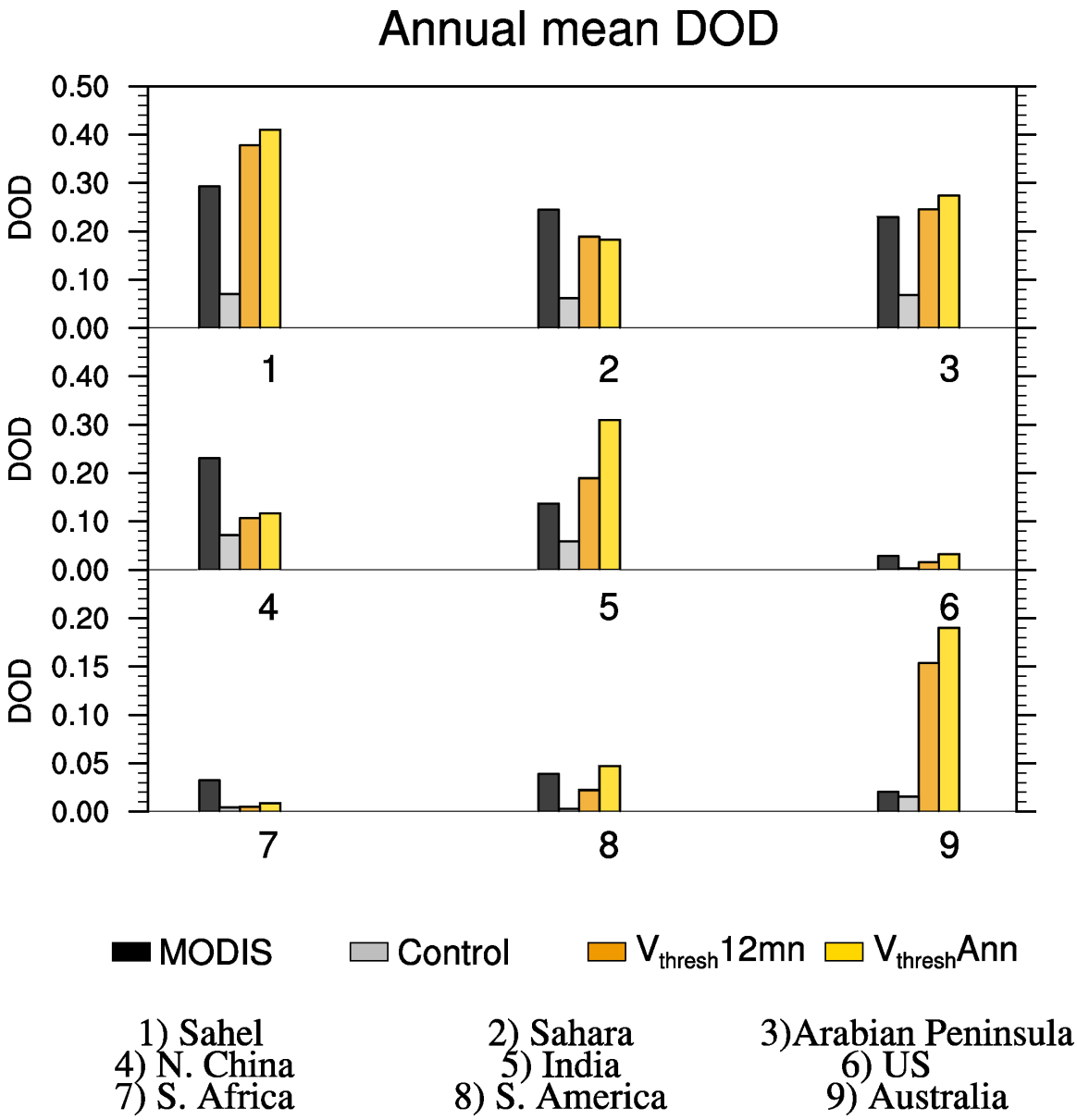

1647 Figure 8. Regional averaged annual mean DOD (2003-2015) over nine regions from the
1648 Control (grey), V_{thresh}12mn (orange), and V_{thresh}Ann (yellow) simulations and MODIS
1649 (black).
1650
1651
1652
1653
1654

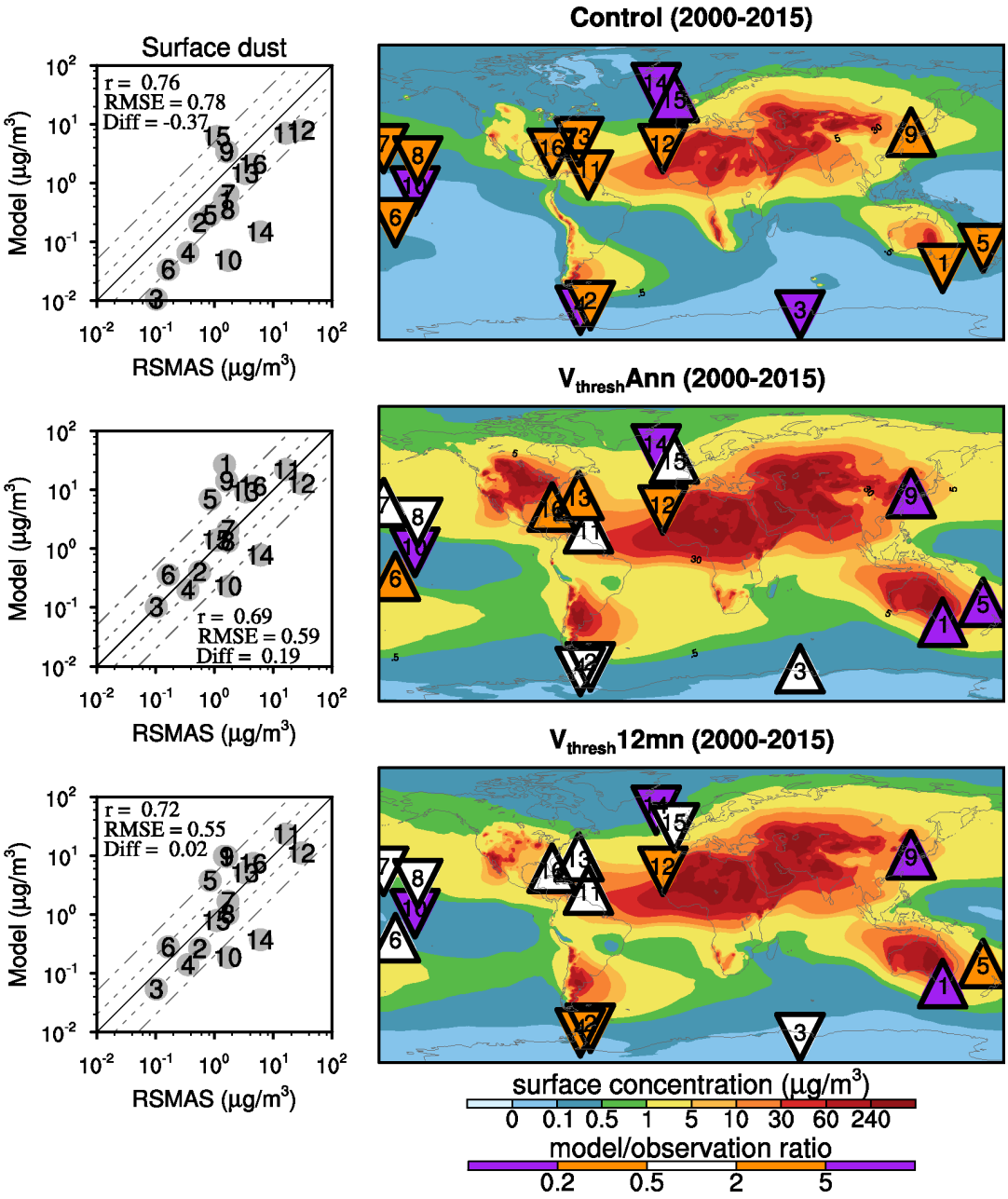

Figure 9. Scatter plots (left column) of model simulated (from top to bottom are the Control, V_{thresh}Ann, and V_{thresh}12mn simulations) surface dust concentration (μg m^{-3}) versus the climatology of observed surface dust concentration from RSMAS stations (Savoie and Prospero 1989), and spatial pattern of surface dust concentration from model output (shading; right column) and the ratio between modeled and RSMAS station observed surface dust concentration (color triangles, with upward triangles indicating overestimation and downward triangles indicating underestimation). 16 stations were used, and numbers in each triangle (right) and grey dots (left) indicate the stations. The one-one, one-two and one-five lines are plotted in solid, dashed and dash-dotted lines in the scatter plots. Statistics in the scatter plots are calculated in logarithmic space.

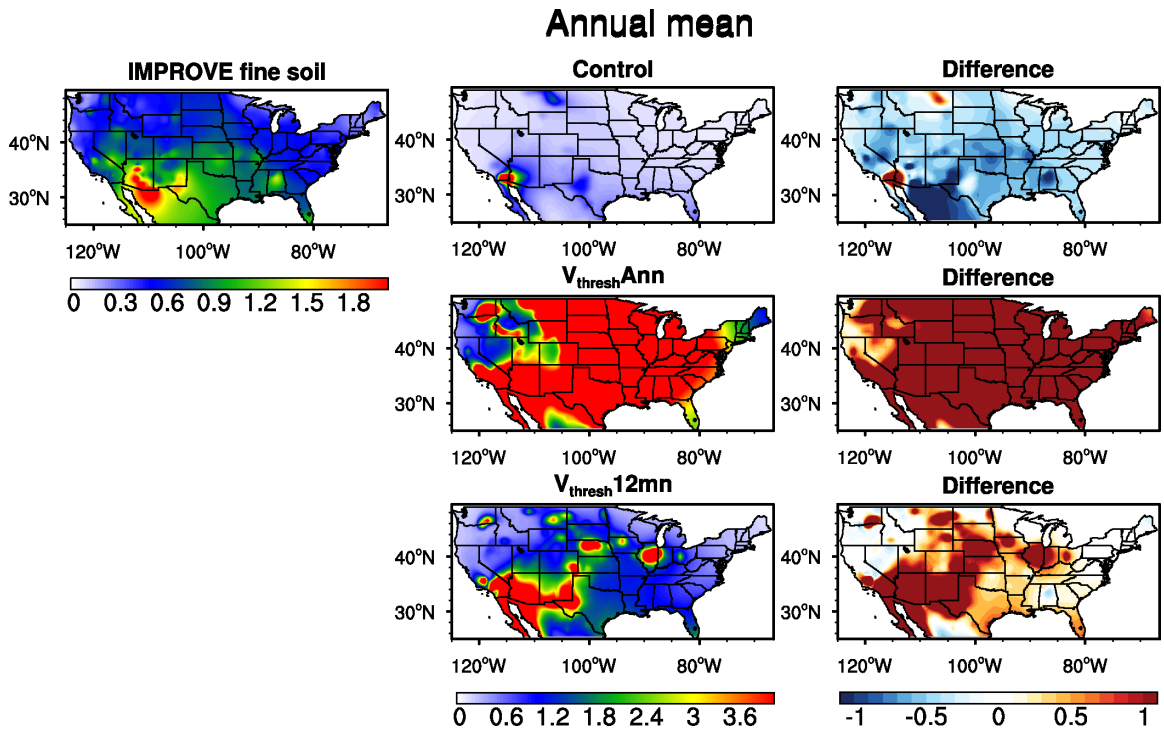

Figure 10. Annual mean surface fine dust concentration (μg m^{-3}) from IMPROVE stations (left column) and three simulations (middle column) and the differences between model and observation (right column) for 2002-2015.

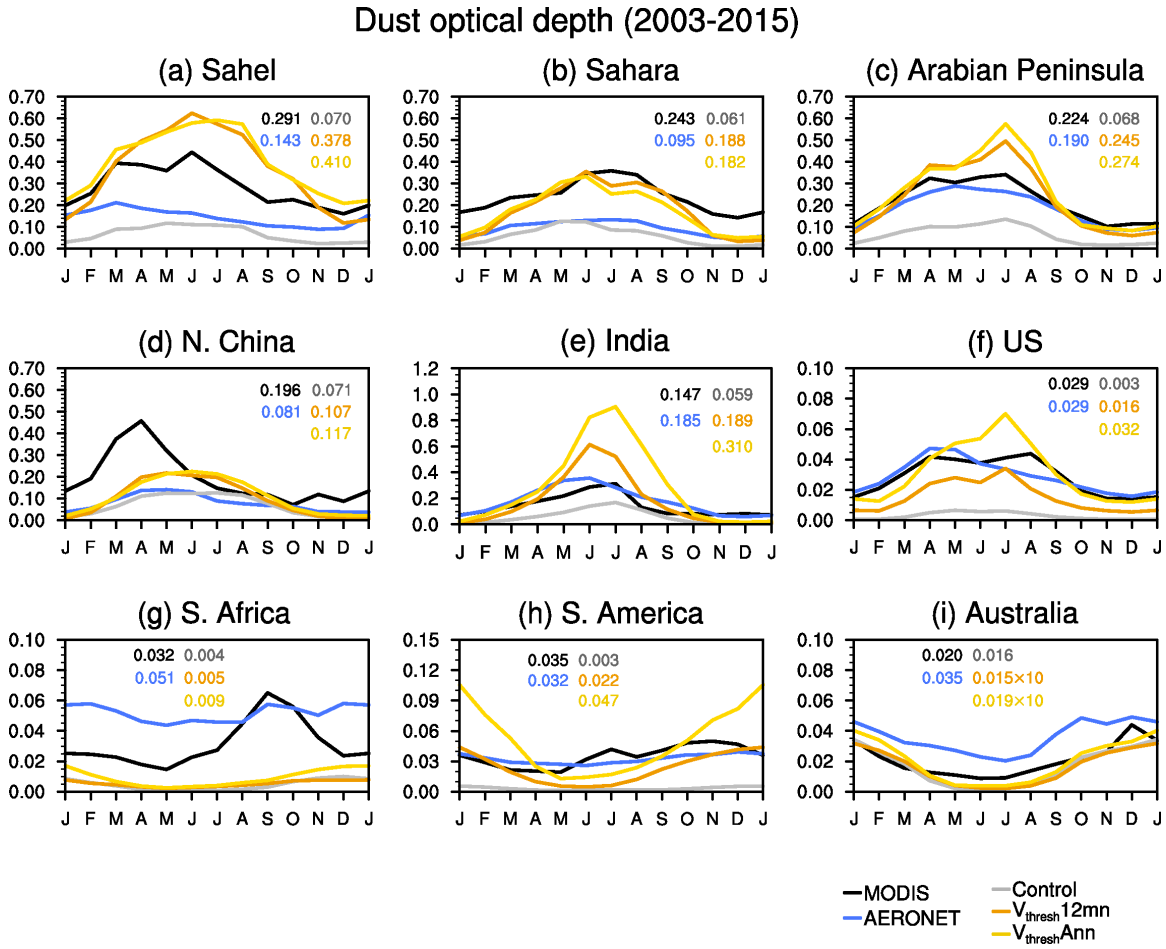

Figure 11. Seasonal cycle of DOD from MODIS (black), the Control (grey), V_{thresh}12mn (orange), and V_{thresh}Ann (yellow) runs, and gridded AERONET SDA COD (blue) averaged over nine regions. The annual mean of each dataset in each region is listed on the top of the plot.

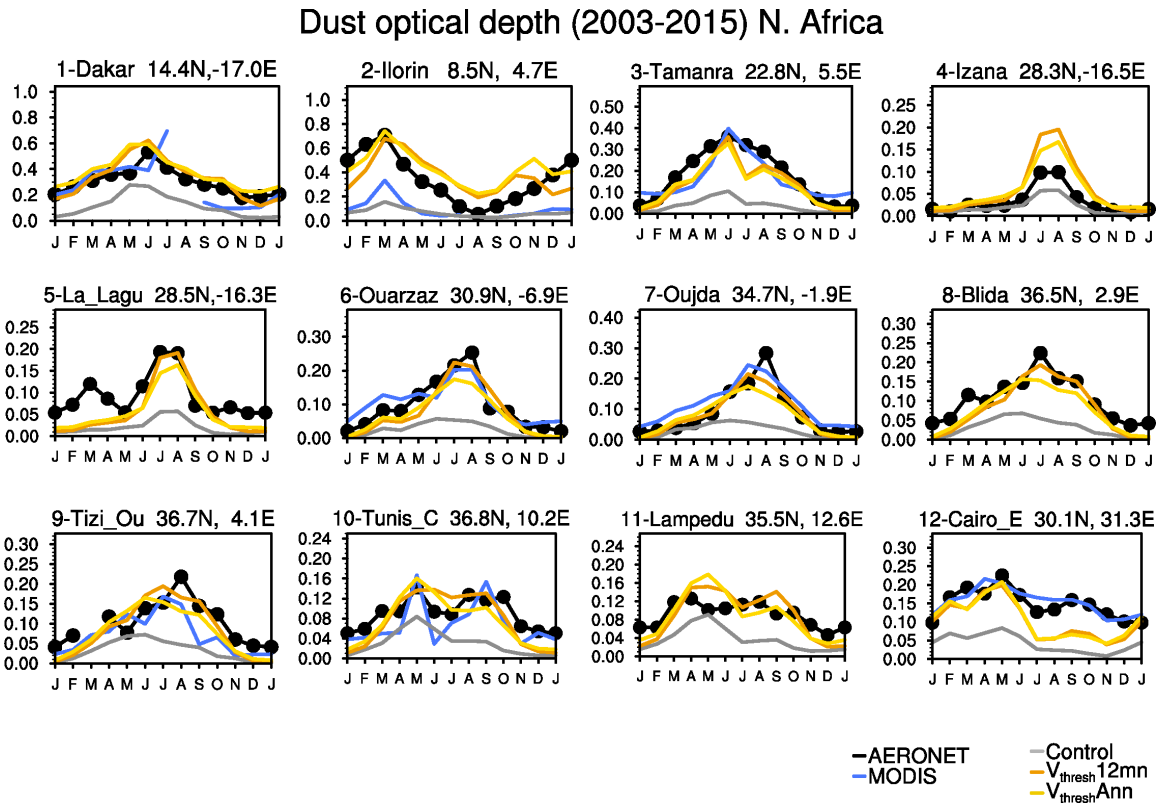

Figure 12. Seasonal cycle of DOD over 12 AERONET SDA sites (see Fig. S7 in the Supplement for locations) from the Control (grey), V_{thresh}12mn (orange), and V_{thresh}Ann (yellow) simulations, along with DOD from MODIS (blue), and COD from AERONET (black dotted line). All values are averaged over 2003-2015. The location (lat/long) and the name (due to space, only first seven characters are shown) of the sites are listed at the top of each plot.

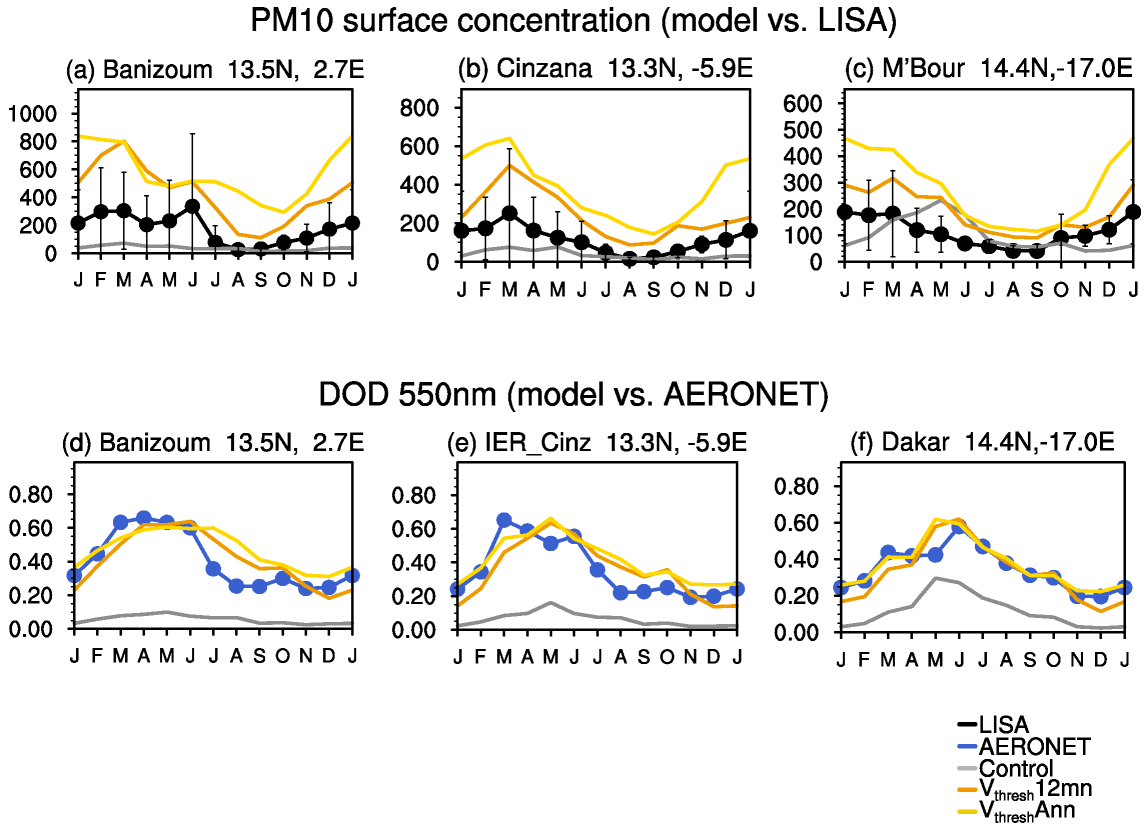

Figure 13. (a)-(c) Seasonal cycle of PM_{10} surface concentration (black) over three sites from the LISA project, along with PM_{10} surface dust concentration from the Control (grey), $V_{thresh}12mn$ (orange), and $V_{thresh}Ann$ (yellow) simulations. Error bars are ± one standard deviations of daily mean in each month averaged over 2006-2014. Unites: $\mu g\ m^{-3}$. (d)-(f) seasonal cycle of DOD (550 nm) from three AERONET sites co-located with LISA sites (blue) versus that modeled by the Control (grey), $V_{thresh}12mn$ (orange), and $V_{thresh}Ann$ (yellow) simulations.

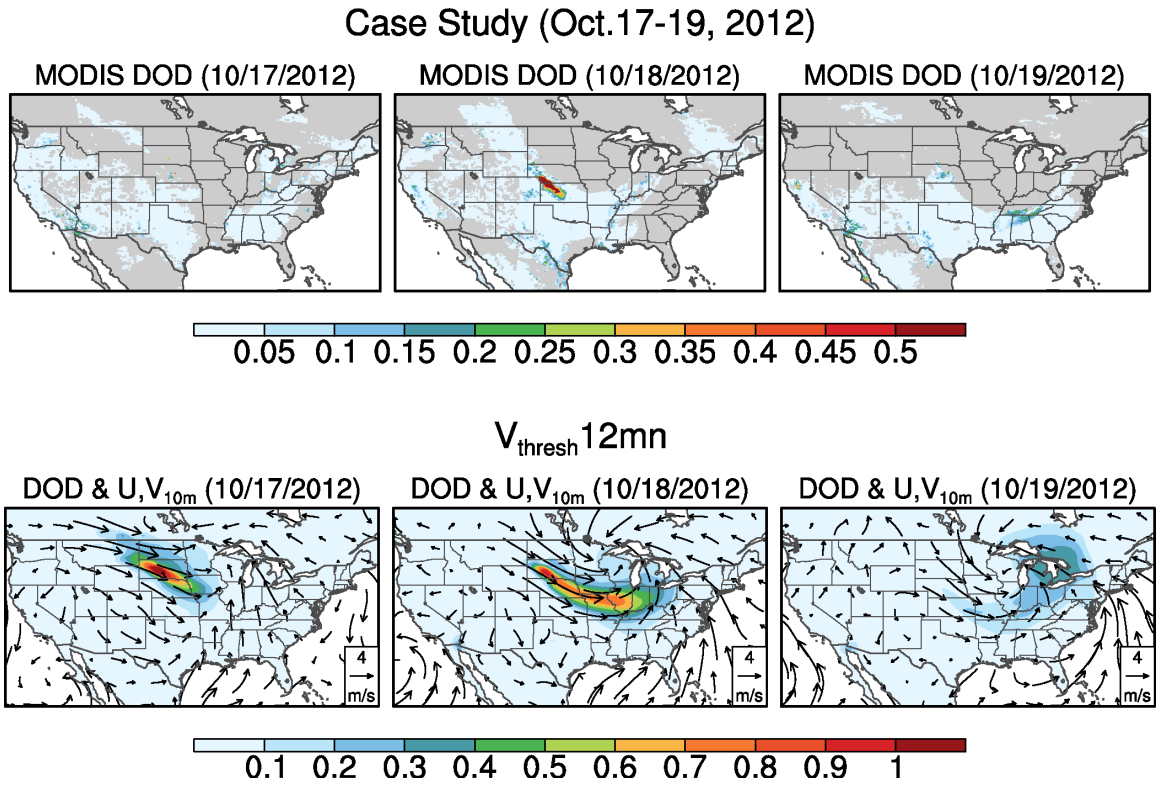

Figure 14. Daily DOD from MODIS (top panel), daily DOD simulated by the V_{thresh}12mn run along with anomalies (with reference to the 2000-2015 mean) of surface wind vectors (m s^{-1}; bottom panel) from Oct. 17th to Oct. 19th, 2012. Only DOD over land is shown. Missing values in MODIS DOD (top panel) are plotted in grey shading.

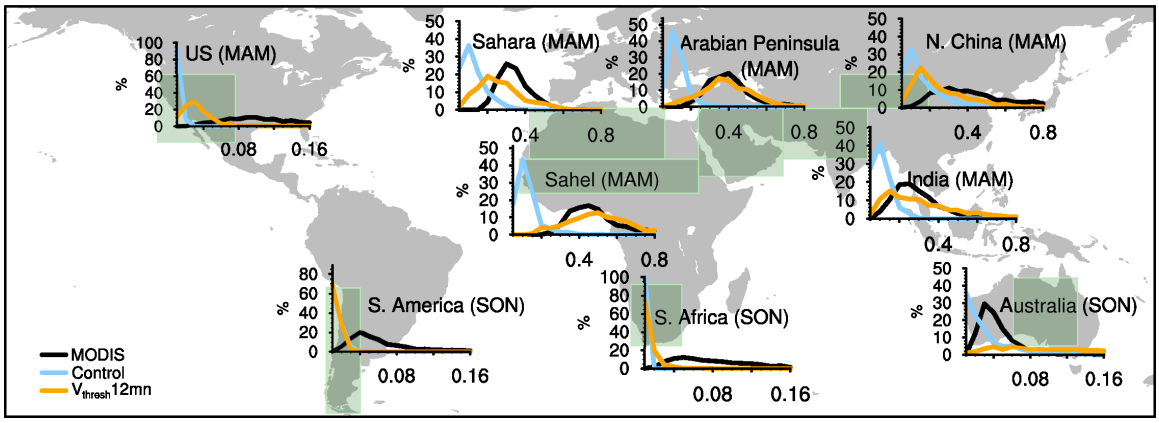

Figure 15. Frequency (%) distribution of regional averaged daily DOD from MODIS (black) versus that from the Control (light blue) and V_{thresh}12mn (orange) simulations for the Sahara, the Sahel, the Arabian Peninsula, northern China, India, western to central U.S., South America, South Africa, and Australia from 2003 to 2015. X-axis denotes the ranges of DOD (the bin spacing for dusty regions is 0.05 and for less dusty regions is 0.01), and y-axis is percentage of occurrence. The light green boxes denote the averaging areas. For regions in the Northern Hemisphere frequency in MAM is shown, while for regions in the Southern Hemisphere frequency in SON is shown.